Applying 3D correlative structured illumination microscopy and X-ray tomography to characterise herpes simplex virus-1 morphogenesis

Kamal L. Nahas[1,2], Viv Connor[1], Kaveesha J. Wijesinghe[1,3], Henry G. Barrow[1], Ian M. Dobbie[4,5], Maria Harkiolaki[2,6*], Stephen C. Graham[1*], Colin M. Crump[1*]

[1]Department of Pathology, University of Cambridge, Tennis Court Road, Cambridge CB2 1QP, United Kingdom

[2]Beamline B24, Diamond Light Source, Harwell Science and Innovation Campus, Didcot OX11 0DE, United Kingdom

[3]Present address: Department of Chemistry, Faculty of Science, University of Colombo, Sri Lanka

[4]Micron Advanced Bioimaging Unit, Department of Biochemistry, University of Oxford, South Parks Road, Oxford, OX1 3QU, United Kingdom

[5]Integrated Imaging Center, Department of Biology, Johns Hopkins University, 3400 N. Charles St., Baltimore, Maryland, 21218, United States of America

[6]Present address: Department of Chemistry, University of Warwick, Coventry, CV4 7AL, United Kingdom

* maria.harkiolaki@warwick.ac.uk (MH); scg34@cam.ac.uk (SCG); cmc56@cam.ac.uk (CMC)

ORCIDs: KLN 0000-0003-3501-8473; MH 0000-0001-8091-9057; SCG 0000-0003-4547-4034; CMC 0000-0001-9918-9998

Contributions: Conceptualization: KLN, MH, SCG, CMC; Data Curation: KLN; Funding Acquisition: MH, SCG, CMC; Investigation: KLN, VC, KJW, HGB, MH, SCG, CMC; Project Administration: MH, SCG, CMC; Resources: IMD, MH; Software: KLN, IMD; Supervision: MH, SCG, CMC; Visualization: KLN; Writing – Original Draft Preparation: KLN; Writing – Review & Editing: KLN, MH, SCG, CMC

Short Title: Correlative light X-ray tomography of herpesvirus assembly

Keywords: Herpesvirus, correlative imaging, cryoSXT, cryoSIM, envelopment

Importance

To date, the characterisation of HSV-1 mutants in the study of virus assembly has been limited to transmission electron microscopy (TEM) without the addition of correlative light microscopy to identify fluorescently labelled viral proteins. In addition, only a small number of mutants are typically used in each study. Herein, a comparative analysis of nine HSV-1 mutants lacking specific structural proteins was performed using correlative fluorescence microscopy and X-ray tomography for the first time, revealing the relative roles of each viral protein in virus assembly. pUL11, pUL51, gK, and gE were shown to have important roles in cytoplasmic envelopment, with the loss of their functions leading to various stalled cytoplasmic envelopment phenotypes involving polarised arrays of capsids at one side of cytoplasmic vesicles that to our knowledge have never been seen with TEM. This correlative imaging approach enabled the study of cytoplasmic envelopment in 3D, revealing an envelopment mechanism driven by capsid budding rather than membrane wrapping. Further cryoSIM experiments revealed that pUL16 and pUL21 are important in nuclear egress of HSV-1 and that VP16 promotes nuclear egress and delivery of capsids to cytoplasmic envelopment compartments. By providing novel and comparative insights into the roles of different viral proteins in various stages of HSV-1 assembly, these findings highlight the utility of correlative cryo-fluorescence plus cryo-soft-X-ray tomography for probing trajectories of intracellular pathogen assembly.

Abstract

Numerous viral genes are involved in assembly of herpes simplex virus-1 (HSV-1), but their relative importance and function remain poorly characterised. Transmission electron microscopy has been used to study viral protein function in cells infected with HSV-1 mutants; however, these studies were usually conducted without correlative light microscopy to identify specific viral components. In this study, fluorescent capsid (eYFP-VP26) and envelope (gM-mCherry) proteins were imaged by structured illumination microscopy under cryogenic conditions (cryoSIM) and cellular ultrastructure was captured from the same infected cells using cryo-soft-X-ray tomography (cryoSXT). Nine fluorescent HSV-1 mutants, each lacking a different viral protein, were compared to assess the importance of viral proteins in different stages of HSV-1 morphogenesis. The relative importance of five viral proteins to nuclear egress were ranked (pUL34 > pUL21 > VP16 > pUL16 > pUS3) according to the levels of attenuation observed for each virus. Correlative imaging also revealed the roles of five viral proteins in cytoplasmic envelopment. VP16 was found to be important in capsid delivery to envelopment compartments, while cytoplasmic clusters of virus particles plus features of stalled envelopment not previously described were observed in the absence of pUL11, pUL51, gK, and gE. Finally, this 3D imaging approach was used to capture different assembly stages during cytoplasmic envelopment and to determine that envelopment occurs by particle budding rather than wrapping. The findings demonstrate that tomographic 3D correlative imaging is an emerging technology that sheds new light on viral protein functions and virion morphogenesis.

Introduction

Herpes simplex virus 1 (HSV-1) is a large, enveloped DNA virus from the family *Orthoherpesviridae* that infects mucosal epithelial cells in oral or genital regions and subsequently establishes life-long latent infections in trigeminal and sacral ganglia, respectively[1,2]. HSV-1 is composed of three layers: a proteinaceous capsid that contains the DNA genome, an amorphous layer of at least 23 different proteins known as the tegument, and a lipid bilayer envelope studded with viral glycoproteins[3–8]. Virion assembly involves a complex multi-step pathway in the cell, beginning with the expression of immediate-early viral genes[9]. This is followed by replication of viral DNA, assembly of capsids, and packaging of DNA genomes to form nucleocapsids, all within the nucleoplasm[10]. Given that nucleocapsids are too large to pass through the channels of nuclear pore complexes, they cross the nuclear envelope in a process known as nuclear egress. This begins with budding of nucleocapsids into the perinuclear space through the inner-nuclear membrane (primary envelopment). Once in the perinuclear space, the nucleocapsids possess a temporary envelope, acquired from the inner-nuclear membrane, which will then fuse with the outer-nuclear membrane to release the capsid into the cytoplasm[11–14]. Tegument proteins begin being deposited on the nucleocapsid in the nucleus and this process continues in the cytoplasm[4]. Cytoplasmic nucleocapsids undergo (secondary) envelopment at cytoplasmic endomembranes, such as *trans*-Golgi network vesicles and/or recycling endosomes[5,15], hereafter referred to as cytoplasmic envelopment. This results in the enveloped virion being located in the lumen of a carrier vesicle, which fuses with the plasma membrane to release the virion[4].

The large DNA genome of HSV-1 encodes at least 84 proteins, many of which have uncharacterised functions in virus assembly and differ in the degree of their importance during morphogenesis[5]. HSV-1 mutants lacking expression of specific viral proteins or domains thereof have been used to study the role of viral genes in assembly using 2D transmission electron microscopy (TEM). Several phenotypes associated with attenuation have been observed with this technique, including varying numbers of capsids between the nucleus and cytoplasm, clusters of perinuclear virus particles, and stalled envelopment of cytoplasmic nucleocapsids[16–21]. However, the extensive sample processing associated with TEM (i.e. chemical fixation, dehydration, hardening by resin-embedding or high-pressure freezing, sectioning, and staining) can distort ultrastructure and complicate interpretation of features that appear to show attenuation in virus assembly[22,23]. Thin sectioning also limits our understanding of the 3D nature of phenotypes associated with attenuation in virus assembly[24]. Volumetric ultrastructural imaging of numerous HSV-1 mutants in near-native conditions is needed to draw direct comparisons between viral proteins and to understand the 3D nature of stalled assembly.

In this study, the roles of nine HSV-1 genes in virus assembly were investigated using an emerging 3D correlative imaging strategy consisting of structured illumination microscopy on cryopreserved samples

(cryoSIM) and cryo-soft-X-ray tomography (cryoSXT)[25]. HSV-1 assembly intermediates have previously been observed by cryoSXT without performing cryoSIM, which limited characterisation of virus assembly[26]. Using this correlative light X-ray tomography (CLXT) approach, we employed recombinant viruses expressing fluorescently labelled viral proteins of the capsid (VP26) and the envelope glycoprotein M (gM) to distinguish between unenveloped and enveloped particles in order to study different stages of virion assembly[27–29]. Our study provides an extensive and comparative ultrastructural analysis of herpesvirus morphogenesis, revealing new insights into the virion assembly pathway of these structurally complex viruses.

Results

Generation of mutants to study HSV-1 assembly

HSV-1 particles contain three layers: capsid, tegument, and envelope. A dual-fluorescent KOS strain HSV-1 mutant containing eYFP-tagged capsids and mCherry-tagged envelopes — hereafter referred to as the dual-fluorescent parental (dfParental) virus — was used to enable the independent identification of capsids and envelope and thus distinguish between unenveloped and enveloped particles. The tagged virus encodes eYFP conjugated to the N terminus of the small capsid protein VP26[27–29]. This tagging theoretically allows identification of all virus particles except capsid-free “light” particles[30] in the cytoplasm and immature procapsids in the nucleus that have yet to acquire VP26[31]. The C terminus of the envelope glycoprotein gM was conjugated to mCherry, enabling identification of gM-containing endomembranes plus viral envelopes[29] (**Fig. 1A**). The dfParental virus was used as the template strain to generate nine HSV-1 mutants lacking specific HSV-1 structural proteins. Mutants were generated to study phenotypes associated with an attenuation of virus assembly caused by the loss of specific viral proteins (**Fig. 1A**).

Nine mutants containing single-gene “knockouts” were generated either by introducing stop codons or by sequence deletion (**Fig. 1B**). As pUL34, VP16 and gK are all essential for virion assembly, the ΔUL34, ΔVP16, and ΔgK viruses were cultured using complementing cell lines to generate infectious virions that carry the corresponding protein but are unable to synthesise it, such that virus entry and gene expression could occur as normal, but the protein would be absent during virus assembly. Protein levels of the corresponding knockout genes were undetectable in Vero cells infected with each of the HSV-1 mutants by immunoblot (**Fig. 1C–D**). No suitable antibody was available to detect gK expression and so the presence of the inserted stop codons was confirmed by PCR amplification of the relevant region of the HSV-1 genome and Sanger sequencing (**Supp. Fig. 1A–B**). Furthermore, immunoblotting for pUL20, the obligate binding partner of gK, revealed substantially reduced pUL20 expression in cells infected with the ΔgK mutant (**Fig. 1C**) as previously observed for independent gK deletion mutants[32]. The intensity of the pUS3 bands were reduced for the ΔpUL21 and ΔUL34 mutants (**Fig. 1C**). The US3

gene has a propensity to mutate in response to pUL21 deletion[33], but this was not known at the time these virus stocks were generated, and the ΔpUL21 virus was not grown in a complementing cell line.

Replication kinetics and cell-to-cell spread of HSV-1 mutants

Replication kinetics for all the dual-fluorescent viruses were compared over 24 hours in single-step growth curves (**Fig. 2A** and **Supp. Fig. 2**). These data were compared with measurements of plaque size 72 hours post infection (hpi) that served as collective indicators of attenuation in both replication and cell-to-cell spread (**Fig. 2B–C**). In line with previous work showing that gE is more important in cell-to-cell spread than in virus assembly[7,34–36], defects in replication of the ΔgE virus were not detected in the replication curves (**Fig. 2A**), but the plaque sizes of this mutant were significantly reduced compared with dfParental (**Fig. 2B–C**). gE interacts with a complex of the tegument proteins pUL11, pUL16 and pUL21, providing one route to link the tegument and envelope layers during virus assembly[37–41]. Replication of the ΔpUL11, ΔpUL16, and ΔpUL21 mutants was generally reduced with respect to dfParental HSV-1 (10–100-fold reduction), suggesting these proteins have more important roles than gE during virion assembly and could perform these roles as a complex (**Fig. 2A**). ΔpUL11 and ΔgE plaques were significantly smaller than the ΔpUL16 and ΔpUL21 plaques, suggesting the interactions formed by pUL11 and gE are more important for cell-to-cell spread (**Fig. 2B–C**)[42]. However, viruses lacking functional pUL21 are known to form extremely small plaques and compensatory mutations in the US3 gene can arise when pUL21 is inactivated[33]. The sequence of US3 in the ΔpUL21 virus was therefore analysed by PCR and Sanger sequencing, revealing that 84.3% of ΔpUL21 genomes encoded an amino acid substitution (C456T) in the US3 gene (**Supp. Fig. 3A–C**). Residues with similar physicochemical properties (e.g. serine) are present at this position in US3 from other alphaherpesviruses, suggesting that this substitution is unlikely to severely alter US3 activity (**Supp. Fig. 3D–E**). Although the residue is surface exposed (**Supp. Fig. 3F**), it is not located near the active site, suggesting it is unlikely to affect kinase activity (**Supp. Fig. 3G**). Nonetheless, potential alterations to pUS3 activity in the ΔpUL21 mutant should be taken into account when the results for this mutant are interpreted.

After capsid assembly in the nucleus, capsids migrate into the cytoplasm by budding into the perinuclear space through the inner-nuclear membrane, forming a temporarily enveloped particle[43]. The envelope of the perinuclear particles fuses with the outer-nuclear membrane to release the capsid into the cytoplasm. pUL34 is required for budding into the perinuclear space, and pUS3 is thought to regulate this process via phosphorylation of the pUL31/pUL34 nuclear egress complex (NEC)[44–46]. While replication of the ΔUS3 virus was 10-fold reduced with respect to dfParental at 24 hpi, the plaques formed by the ΔUS3 mutant were closer in size to dfParental plaques than any other mutants at 72 hpi, suggesting that pUS3 had the least important role of all nine mutants for capsid migration into the cytoplasm and subsequent viral spread (**Fig. 2A–C**). In contrast, the replication kinetics of the ΔUL34

mutant were approximately 10^5-fold reduced, and the mutant did not form plaques, which was expected for an essential component of the NEC (**Fig. 2A–C**)[11,12].

VP16, pUL51, and gK are highly important for cytoplasmic envelopment of HSV-1 capsids[8,47–50]. By 24 hpi, replication of the ΔpUL51 virus was 10 to 500-fold reduced and plaque sizes were greatly reduced as well (**Fig. 2A–C** and **Supp. Fig. 2**). Replication kinetics of the ΔgK virus were 10^3 to 10^5-fold reduced at 24 hpi, and no plaques were visible at 72 hpi (**Fig. 2A–C** and **Supp. Fig. 2**). This suggests gK is important in cell-to-cell spread as well as virion assembly. It is possible that infectious ΔgK virions were produced but unable to egress from the cell. In this scenario, infectious particles could be detected in cell lysates generated for titration of the replication curves despite an inability of ΔgK HSV-1 to form plaques. In contrast to the ΔgK mutant, the ΔVP16 mutant produced detectable plaques by 72 hpi even though infectious virions could not be detected by 24 hpi with the replication curves, suggesting the lack of VP16 could delay to beyond 24 hours the production of detectable titres of infectious virus (**Fig. 2A–C**). Alternatively, it is possible that loss of VP16 leads to low levels of cell-cell fusion to form small syncytia, enabling cell-to-cell spread of viral genome and subsequent plaque formation[21].

Correlative light X-ray tomography of HSV-1 assembly

After generating and characterising the mutants, defects in virus assembly were explored with high-resolution imaging techniques under cryogenic conditions. Cryogenic imaging using soft-X-ray tomography captures the ultrastructure of the cell in 3D and has the advantage of allowing the study of samples in a near-native state without the need for chemical fixation[26,51]. U2OS osteosarcoma cells were used in this study because they have been used for ultrastructural HSV-1 research and have been demonstrated to be durable under X-ray exposure (**Fig. 3A**)[26,52,53]. U2OS cells were infected at MOI = 2 with dfParental or mutants for 15.5 hours and were stained with MitoTracker Deep Red (Thermo Fisher Scientific) for 30 minutes to label the mitochondria[54]. Gold fiducials were added to the surface of the cells to facilitate alignment of tomographic projections[54]. Samples were cryopreserved by plunge cryocooling in liquid ethane at 16 hpi. In a synchronously-infected population, infected cells will progress through stages of virus assembly at different rates[26,29,55]. Cells were cryopreserved at a relatively late timepoint (16 hpi) to increase the proportion of cells at late stages of infection. Infected cells were first imaged by cryoSIM to capture viral eYFP-VP26 and gM-mCherry fluorescence plus MitoTracker mitochondrial fluorescence (**Fig. 3B**)[25,56]. These same infected cells were later imaged by cryoSXT. Given that mitochondria produce high contrast in cryoSXT tomograms and are easily distinguishable based on their complex shapes and arrangements[26], the MitoTracker stain in the cryoSIM and the mitochondria in the tomograms were used as landmarks to guide 3D image alignment for correlation[25]. CLXT was used to identify virus particles at various stages of assembly. The nucleus is the site of capsid assembly and nuclear capsids have previously been observed in the tomograms as dark puncta[26]. These capsids correlated with the fluorescently tagged capsid protein eYFP-VP26 (**Fig. 3C**). gM-mCherry$^+$ vesicles and virus particles were detected in the cytoplasm, enabling the study of

cytoplasmic envelopment. Finally, eYFP-VP26+ and gM-mCherry+ particles were detected in spaces between cells, allowing study of extracellular virions (**Fig. 3C**).

Nuclear egress attenuation of ΔpUL16, ΔpUL21, ΔUL34, ΔVP16, and ΔUS3 HSV-1

Nuclei of samples infected with dfParental, ΔpUL16, ΔpUL21, ΔUL34, ΔVP16, and ΔUS3 viruses were labelled with Hoechst stain to distinguish between nuclear and cytoplasmic capsids by cryoSIM (**Fig. 4A**). The plasma membrane of infected cells was delineated by digitally oversaturating the gM-mCherry fluorescence. The number of eYFP-VP26^{+} pixels in maximum Z projections of the cryoSIM data were quantitated using these nuclear and plasma membrane borders. The nuclear:cytoplasmic (N:C) ratio of capsids was used as measures of nuclear egress attenuation, which could manifest from a defect in nuclear egress or a delay in the replication kinetics of mutants (**Fig. 4B**). Infected cells were included in the analysis if the nucleus and cell borders could be easily distinguished, if most of the cell was in the field of view, and if most of the gM-mCherry^{+} areas of the cytoplasm did not overlap with the nucleus. However, partial overlap between gM-mCherry fluorescence and the nucleus was common (e.g. ΔpUL21 and ΔUL34 in **Fig. 4C**), which could have produced an overestimated N:C ratio. These data demonstrated that ΔpUL16, ΔpUL21, ΔUL34, ΔVP16, and ΔUS3 viruses experienced a defect or a delay in nuclear egress when compared with the dfParental virus (**Fig. 4B–C**). The ΔgE virus was included in the analysis as a negative control because this virus did not have delayed replication kinetics (**Fig. 2A**), and gE is not suspected to be involved in nuclear egress. The ΔgE virus-infected cells were not stained with Hoescht, and instead the nucleus was identified using images of nuclei collected from tiled X-ray projection images (X-ray mosaics). The N:C ratio of the dfParental (N=14) and ΔgE (N=12) viruses did not differ significantly, suggesting gE does not play a role in nuclear egress. pUL34 is essential for nuclear egress and served as a positive control for nuclear capsid retention in this study[11,12]. The ΔUL34 virus had the highest N:C ratios (N=10; **Fig. 4B–C**), which was commensurate with the high level of attenuation observed for this virus in terms of replication kinetics and its inability to form plaques (**Fig. 2A–C**). For the other mutants, significance in difference was assessed with respect to the N:C ratios of both the dfParental and ΔUL34 viruses. Although the N:C ratios of the ΔUS3 virus (N=13) were significantly higher than those of the dfParental virus, they were also significantly lower than those of the ΔUL34 virus. The ΔUS3 virus had the lowest N:C ratios of the mutants other than the ΔgE negative control (**Fig. 4B–C**), suggesting ΔUS3 was least attenuated in nuclear egress, which is commensurate with its modest attenuation in the replication curves and plaque size assay (**Fig. 2A–C**). ΔpUL16 (N=13) and ΔpUL21 (N=11) N:C ratios were significantly higher than those of the dfParental virus but were not significantly different from those of the ΔUL34 virus (**Fig. 4B–C**), suggesting a greater defect or delay in nuclear egress than observed for ΔUS3 and consistent with known roles for both proteins in nuclear egress of HSV-2[18,20,57]. N:C ratios of ΔVP16 (N=24) were also significantly greater than those of dfParental, suggesting a defect or delay in nuclear egress (**Fig. 4B–C**), consistent with TEM studies implicating VP16 in nuclear egress[21,58]. CryoSIM data from infected

cells were correlated onto X-ray tomograms, revealing an absence of, or reduction in, cytoplasmic capsids for each of the five mutants (**Fig. 4D**).

Differential capsid clustering and gM-mCherry^{+} endomembrane association of ΔpUL11, ΔpUL51, ΔgE, ΔgK, and ΔVP16 mutants

CryoSIM imaging showed that interspersed eYFP-VP26+ capsids and gM-mCherry+ endomembranes could be observed at juxtanuclear assembly compartments (JACs) in cells infected with dfParental (**Fig. 5A**). Varying degrees of attenuation in cytoplasmic envelopment have been previously reported for HSV-1 mutants lacking some of the tegument proteins or glycoproteins investigated in this study (i.e. pUL11[16,17,59], VP16[21], pUL51[48,49,60], gK[47,61], and gE[36,42]), and some proteins have been proposed to participate in cytoplasmic envelopment (i.e. pUL16[37] and pUL21[62,63]). For cells infected with ΔpUL11, ΔpUL51, ΔgK, or ΔgE, clusters of capsids could be observed at the JACs (**Fig. 5C**). Smaller clusters of capsids were observed in the JACs for the ΔpUL11 and ΔgE mutants (**Fig. 5C**), whereas more extensive clusters of capsids were observed in the JACs for the ΔpUL51 and ΔgK. Capsid clustering was not observed in cells infected with ΔVP16 virus, and cytoplasmic capsids appeared to associate less with gM-mCherry+ endomembranes compared with capsids of dfParental, suggesting VP16 is important in capsid recruitment to envelopment compartments (**Fig. 5B–C**). The spatial distribution of capsids in the cytoplasm of cells infected with ΔpUL16 and ΔpUL21 could not be reliably assessed due to a paucity of cytoplasmic capsids detected, presumably arising from their observed defect/delay in nuclear egress (**Fig. 4B-D**).

To quantitate cytoplasmic distribution of virus particles, the intensity of gM-mCherry fluorescence was used to delineate the approximate borders of JACs (**Fig. 5A**). dfParental capsids in these assembly compartments associated closely with gM-mCherry^{+} endomembranes. However, cells infected with the ΔVP16 virus contained fewer capsids in the JAC and they were less closely associated with gM-mCherry^{+} endomembranes (**Fig. 5A–C**). Thresholds on intensity were applied to the eYFP-VP26 and gM-mCherry cryoSIM fluorescence to produce binary masks where noise and background were filtered out. The ratio of eYFP-VP26^{+} pixels to gM-mCherry^{+} pixels in the binary masks was measured for each JAC and were significantly lower for the ΔVP16 virus when compared with dfParental (**Fig. 5D**), indicating fewer capsids at the JAC for this virus. This is consistent with the lack of overlap between capsids and gM-mCherry+ endomembranes observed (**Fig. 5B**) plus the observed defect/delay in nuclear egress (**Fig. 4B–D**). ΔUS3 was included in the analysis as a negative control for a virus with impaired nuclear egress that is not expected to be attenuated in cytoplasmic envelopment. The ratio of eYFP-VP26^{+} pixels to gM-mCherry^{+} pixels at the JACs was not significantly different between the dfParental and ΔUS3 viruses (**Fig. 5D**), suggesting that the lower ratio of eYFP-VP26^{+} pixels to gM-mCherry^{+} pixels in the JAC of ΔVP16 infected cells reflects poor capsid recruitment to these compartments in the absence of VP16. The eYFP-VP26^{+} pixels to gM-mCherry^{+} pixels ratio for the ΔpUL11, ΔpUL51, and ΔgE mutants was not significantly different from dfParental, suggesting capsid

recruitment was unimpaired, and for ΔgK this ratio was significantly increased, suggesting that capsid recruitment to or retention at JACs is enhanced in cells infected with this mutant (**Fig. 5D**).

Colocalization analyses were performed to determine the overlap between capsids and gM-mCherry$^+$ endomembranes at the JACs. Manders colocalization coefficients, which are based on spatial coincidence, were chosen over intensity-based measures, such as Pearson's correlation coefficients, to minimize the influence of noise and cryoSIM reconstruction artefacts. Manders coefficient 1 (M_1) was calculated for each JAC and represented the number of eYFP-VP26$^+$ pixels that overlapped with gM-mCherry$^+$ pixels as a proportion of all eYFP-VP26$^+$ pixels. Manders coefficient 2 (M_2) was also calculated for each JAC and represented the number of gM-mCherry$^+$ pixels that overlapped with eYFP-VP26$^+$ pixels as a proportion of all gM-mCherry$^+$ pixels. These two measurements reflect the association of capsids with gM$^+$ endomembranes. Both metrics were significantly lower for the ΔVP16 virus (N=22) compared with dfParental (N=16; **Fig. 5E, Supp. Fig. 4**). The M_1 and M_2 coefficients for the mutants that formed small capsid clusters (i.e. ΔpUL11 [N=25] and ΔgE [N=23]) did not significantly differ from dfParental. For the mutants that form large capsid clusters, the M_1 coefficient was larger than dfParental for both ΔpUL51 (N=17) and ΔgK (N=18) but only reached statistical significance for ΔpUL51, and the M_2 coefficient was increased for both ΔgK and ΔpUL51 but only reached statistical significance for ΔgK. This suggests enhanced association of capsid and gM$^+$ endomembranes in the JAC for both these mutants but with different distributions of the components (**Fig. 5E**).

CLXT imaging provided higher resolution details of the relative capsid and membrane arrangement for these mutants. As observed by cryoSIM (**Fig. 5A**), cytoplasmic clusters of virus particles were not observed for dfParental HSV-1 by CLXT (**Fig. 6A**). Small clusters of virus particles (<10 μm^3) were observed in the JACs of the ΔpUL11 and ΔgE mutants (**Fig. 6B**), and larger clusters of virus particles (≥10 μm^3) were observed in the JACs of the ΔpUL51 and ΔgK viruses (**Fig. 6C**). Additionally, linear arrays of capsids were observed in the cytoplasm of the ΔgK virus (**Fig. 6D**) that were not observed in dfParental-infected cells (**Fig. 3C**). CLXT revealed that these linear capsid arrays are not associated with gM-mCherry$^+$ endomembranes. From their linear organisation we suspect they are located along filaments that could not be reliably resolved by cryoSXT, potentially microtubules as these are known to be important for intracellular capsid transport[64].

3D envelopment mechanism of HSV-1

The high penetrating power of X-rays enables the entire depth of the cell in each field of view to be imaged by cryoSXT, allowing rare or transient events to be captured[26]. Combining this with the HSV-1 mutant strains that have impaired envelopment allows us to enrich intermediate stages of virus assembly that are otherwise extremely rapid and thus difficult to visualise. Numerous independent assembly intermediates of the ΔpUL51 virus were detected by CLXT (**Fig. 7A–B, Supp. Fig. 5A–B**). These included unenveloped capsids in the cytoplasm and capsids embedded in the surface of gM-

mCherry+ vesicles. Note that the anterior and posterior faces of these vesicles cannot be reliably segmented owing to their lower contrast, a result of the 'missing wedge' in the tomographic data acquisition. Such vesicles were enriched in gM-mCherry at the pole near the capsids, indicating that gM-mCherry and potentially other viral proteins become concentrated at microdomains on vesicles prior to envelopment (**Fig. 7A**). This observation is consistent with a previous hypothesis suggesting concentration of tegument and glycoproteins at the 'assembly pole' of the virion[65]. Virus particles budding into vesicles and fully enveloped virions were also observed (**Fig. 7A–B**). Fully enveloped virions were distinguished from budding intermediates by observing differences in voxel intensity across the vesicles that contain them: the virions were separated from the vesicle membrane by a narrow volume of lumenal space that appeared brighter (**Supp. Fig. 5B**), whereas budding events displayed a continuous drop in intensity between the membrane and the budding intermediate (**Supp. Fig. 5A**). A 2D cross-section of a budding event (**Fig. 7C–D**) appears topologically similar to envelopment events observed by 2D TEM (**Fig. 7E**). This 3D view of cytoplasmic budding suggests envelopment is driven by capsid budding into spherical/ellipsoidal vesicles rather than by thin tubular endomembranes forming projections to wrap around capsids.

Capsid arrays were frequently observed near cytoplasmic vesicles for the ΔgK (**Fig. 8A**), ΔpUL11 (**Fig. 8B**), ΔpUL51 (**Fig. 8C**), and ΔgE (**Fig. 8D**) viruses. These features were not observed in dfParental-infected cells (**Fig. 3C**), and they share four phenotypes regardless of the type of mutant. First, an array of capsids is located around one pole of the vesicle but not the antipole. Second, the capsids appear to be near the vesicles but generally do not appear embedded in the surface. Third, the pole of the vesicle near to the capsid arrays appears darker in the tomograms, indicating a greater presence of X-ray absorbing material. Fourth, CLXT revealed the vesicle pole near to the capsid arrays is enriched in gM-mCherry, suggesting gM and potentially other viral proteins accumulate at the pole nearer the capsid arrays, which could account for the greater abundance of X-ray absorbing material. Based on these four shared phenotypes, we interpret these features to represent capsids interacting with appropriate target membranes but experiencing a delay or defect in their ability to bud into the vesicle lumen to acquire an envelope. To our knowledge, stalled envelopment events with these details have not been described by 2D TEM. The 3D nature of cryoSXT increases the likelihood that ultrastructural features such as these could be captured regardless of orientation with respect to the XY projection plane[66].

To quantitate the variation in X-ray absorbing material along the membrane from a stalled envelopment event for each virus, the voxel intensities of 30 points on the relevant vesicles were measured (**Fig. 8E–H**). X-ray tomograms reconstructed by weighted back projection (WBP) were used for the analysis without applying any noise-averaging simultaneous iterations reconstruction technique (SIRT)-like filters[67]. Given that WBP tomograms are noisy[67], voxel intensities were sampled from a 3×3 voxel matrix in the XY plane at each point on the vesicle and the minimum value was used. Voxel intensities were collected and averaged from three tandem tomographic projections spanning a depth of 30 nm. For all four mutants, the voxel intensity was lower on the vesicle pole nearer to the capsid arrays (**Fig. 8E–H**).

Voxel intensity is proportional to the X-ray radiation transmitted through the sample to the detector. A low voxel intensity suggests lower X-ray transmittance and greater X-ray absorption, indicating the vesicle pole nearer the capsid arrays contained a greater amount of carbon-rich X-ray-absorbing material. To visualise the variation in X-ray absorption around the vesicle from **Fig. 8D** in 3D, the voxel intensity of the tomogram was superimposed and false-coloured onto a segmentation of the vesicle (**Fig. 8I**). This illustrated that the vesicle pole nearer the capsid arrays had greater X-ray absorption than the antipole. The width of vesicles associated with capsid arrays were measured using the quantitation program *Contour*[68] and these vesicles had a mean width of 704.9 ± 206.5 nm (mean ± SD, n = 34) (**Supp. Fig. 6A**). Stalled envelopment features were not observed in dfParental-infected cells, and we wondered whether the enrichment of gM-mCherry at one vesicle pole was an artefact of deleting tegument or envelope proteins that could directly or indirectly interact with gM (e.g. pUL11 or gE)[4]. However, polarisation of vesicular gM-mCherry was observed in dfParental-infected cells in the absence of capsid arrays (**Supp. Fig. 6B**). In this case, the vesicle appeared to be constricted in between the gM-mCherry^{+} and gM-mCherry^{-} poles, which could arise for numerous reasons, such as fusion, fission, or pressure imposed by microtubules.

Stalled envelopment was frequently observed for the ΔgE virus (**Supp. Fig. 7A**). This was surprising because no attenuation in replication kinetics was detected for the ΔgE virus when compared with dfParental (**Fig. 2A**). Previous research indicated HSV-1 lacking both gE and gM was more severely attenuated in replication kinetics than HSV-1 lacking one of either protein[69]. This could be related to the indirect interaction between gE and gM via the VP22 tegument protein (**Supp. Fig. 7B**)[69]. Untagged and eYFP-VP26/gM-mCherry-tagged forms of the virus displayed similar replication kinetics, suggesting no detectable impact on replication of mCherry conjugation to the C terminus of gM (**Supp. Fig. 7C**). Plaque sizes were measured for each virus to determine if the tagging affected cell-to-cell spread. The ΔgE virus was on average 0.65× smaller than the WT virus for the untagged form but 0.35× smaller for the tagged form, suggesting the tagging contributed to an attenuation in cell-to-cell spread (**Supp. Fig. 7D–E**).

Width measurements of virus assembly intermediates

Electron cryo-tomography (cryoET) has been used to measure the width of the tegument layer and an asymmetric distribution of tegument around the capsid has been demonstrated, with widths of 5 nm and 35 nm at opposing poles[70]. Widths of viral assembly intermediates were measured for the dfParental, ΔpUL51, and ΔgE viruses by cryoSXT to determine if the added width of the tegument layer around the capsid could be detected (**Fig. 9 & Table 1**)[26]. No difference was observed in the width of nuclear capsids and unenveloped membrane-proximal capsids by cryoSXT (**Fig. 9 & Table 1**). This could indicate that recruitment of tegument to capsids does not occur until cytoplasmic envelopment. However, ICP0, ICP4, pUL36, pUL37, and pUS3 are thought to condense on capsids in the nucleus, demonstrating tegument condensation begins early in assembly[71,72]. Alternatively, it is possible that the

tegument layer is too diffuse around cytoplasmic capsids such that it does not produce detectable X-ray absorption by cryoSXT. Under this scenario, X-ray absorption may become detectable if the tegument layer were to compress around capsids upon membrane-embedding and budding. Embedded particles widths were measured normal (at 90°) to the membrane to limit distortion of the measurements by the membrane. The widths of embedded particles (184.12 ± 4.86 nm SEM; N = 17; range 150–220 nm; SD 20.02 nm) were significantly greater than nuclear capsids (122.48 ± 0.94 nm SEM; N = 149; range 100–150 nm; SD 11.44 nm; Mann-Whitney *U*-test p-value = 4.27×10^{-12}) or membrane-proximal capsids (124.95 ± 1.15 nm SEM; N = 105; range 100–150 nm; SD 11.78 nm; Mann-Whitney *U*-test p-value = 1.79×10^{-11}), suggesting the tegument layer condenses and compresses around the capsid upon membrane-embedding and budding (**Fig. 9 & Table 1**). The widths of embedded particles were also significantly lower than intracellular enveloped particles (216.85 ± 4.65 nm SEM; N = 54; range 160–300 nm; SD 34.19 nm; Mann-Whitney *U*-test p-value = 6.8×10^{-4}) and extracellular particles (210.00 ± 5.65 nm SEM; N = 21; range 180–280 nm; SD 25.88 nm; Mann-Whitney *U*-test p-value = 3.5×10^{-3}), consistent with incomplete membrane acquisition.

Discussion

Application of correlative cryoSIM and cryoSXT imaging to the study of viral infection has thus far been limited to visualising the entry of reovirus during infection and has not yet been used to study other stages of virus assembly, nor has it been used to study phenotypes of mutant viruses[25]. In this study, nine mutants of HSV-1, each lacking a protein involved in virus assembly, were generated to study attenuation in nuclear egress and cytoplasmic envelopment with correlative cryoSIM and cryoSXT imaging. Each mutant genetically encoded fluorescent capsid (eYFP-VP26) and envelope (gM-mCherry) proteins that allowed identification of viral assembly intermediates without the need for chemical fixation, cell permeabilization or immunostaining, all of which could introduce ultrastructural artefacts. Instead, samples were vitrified in a physiologically-relevant near-native state by plunge-cryocooling[66]. Lack of protein expression for each mutant gene was verified (**Fig. 1C–D**); the replication kinetics and plaque sizes for each virus were assessed (**Fig. 2A–C**); roles of pUL16, pUL21, pUL34, VP16, and pUS3 in nuclear egress of HSV-1 were observed (**Fig. 4**); CLXT revealed different phenotypes associated with attenuation for cytoplasmic envelopment with the ΔpUL11, ΔVP16, ΔpUL51, ΔgK, and ΔgE viruses, suggesting the corresponding proteins possess different functions in envelopment (**Fig. 5–8**); and the widths of virus assembly intermediates identified by CLXT were measured (**Fig. 9 & Table 1**).

The large defect in nuclear egress of HSV-1 lacking pUL34 as assessed by cryoSIM and CLXT observation (**Fig. 4B–D**) is consistent with its role as an essential component of the viral NEC. A nuclear egress defect was apparent but was significantly less pronounced for the ΔUS3 mutant, consistent with the impact of pUS3 kinase-regulated NEC activity and nuclear lamina dispersal being variable in magnitude and cell-type specific[46,73–75]. While both pUL16 and pUL21 have been shown to promote nuclear egress in HSV-2[18,57], previous studies have not confirmed a role for either protein in nuclear egress in HSV-1[19,76]. Our cryoSIM and CLXT data (**Fig. 4B–D**) show that both pUL16 and pUL21 promote nuclear egress in U2OS cells. Of note, the ΔpUL21 mutant was found to contain a non-synonymous point mutation in pUS3 that may independently influence nuclear egress **(Supp. Fig. 3),** consistent with our previous data showing positive selection of pUS3 mutations during passage of pUL21 mutant viruses that rescues HSV-1 replication and spread[33]. While the presence of the pUS3 C463T mutation in our eYFP-VP26 and gM-mCherry tagged ΔpUL21 virus may be expected to compensate for any defect in nuclear egress in order to restore viral fitness, the nuclear egress defect observed for the ΔpUL21 mutant is greater than for the ΔUS3 mutant (**Fig. 4B**). This suggests that, if anything, our cryoSIM and CLXT data may underestimate the importance of pUL21 in this process. In addition, we note that our CLXT studies cannot differentiate mature genome-containing 'C' capsids from the genome-free 'A' and 'B' capsids that are known to accumulate in the absence of HSV-1 pUL16[76] and pUL21[19,77]. The reduced extent of nuclear egress at 16 hpi for the ΔVP16 virus (**Fig. 4B–D**) could be attributed to a slower rate of replication in the absence of VP16 (either via diminished immediate-early gene trans-activation[78] or via loss of regulation of the HSV-1 viral host shutoff protein[79]) rather

than an attenuation in nuclear egress. However, the results are consistent with previous research that showed VP16 is incorporated on perinuclear virus particles in HSV-1[58] and that cells infected with a ΔVP16 virus produce clusters of virus particles in the perinuclear space[21]. The significant defect or delay in nuclear egress observed in this study (**Fig. 4B–D**) indicates that VP16 could play a larger role in nuclear egress than previously supposed.

In addition to nuclear egress, the CLXT workflow presented here represents a powerful platform for comparative investigation of viral cytoplasmic envelopment. Substantial cytoplasmic envelopment defects were observed for the ΔpUL11, ΔpUL51, ΔgE, ΔgK, and ΔVP16 mutants (**Fig. 5–6**), but the precise phenotype of the defect differed between mutants. Capsids were largely absent from juxtanuclear gM-mCherry^{+} endomembranes in cells infected with the ΔVP16 virus. This is consistent with the highly-abundant tegument protein VP16 playing a key role in bridging inner tegument proteins with the outer tegument and viral glycoproteins during assembly as well as the severe replication deficiencies of this mutant at 24 hpi (**Fig. 2A**)[50,80–86]. Cells infected with ΔpUL11 and ΔgE HSV-1 had small clusters of capsids in JACs (**Fig. 5 & Fig. 6**), consistent with previous TEM studies[16,17,36,87,88], and both had moderate defects in virus replication and/or spread (**Fig. 2A–C**), suggesting that both play modest roles in cytoplasmic envelopment. Removal of pUL51 or gK gave rise to much larger clusters of capsids (**Fig. 5 & Fig. 6**) and more extensive replication and spread defects (**Fig. 2A–C**), suggesting more severe deficiencies in capsid envelopment. pUL51 and its binding partner pUL7 have established roles in stimulating the cytoplasmic wrapping of nascent virions[49,89], and the 3D structure of pUL51 closely resembles components of the cellular endosomal sorting complex required for transport (ESCRT)-III machinery[48], but the precise molecular roles pUL7 and pUL51 play in capsid envelopment remain unclear. Two replication curves reveal that removal of pUL51 expression causes a wide-ranging 10- to 500-fold reduction in virus replication (**Fig. 2A** and **Supp. Fig. 2**), which is consistent with data showing that inhibition of ESCRT activity via expression of a dominant negative form of the ESCRT-associated cellular ATPase VPS4A effectively prevents HSV-1 budding[90]. CLXT reveals large clusters of cytoplasmic virus particles and stalled envelopment events for ΔpUL51 HSV-1 (**Fig. 5 & Fig. 6**), suggesting that pUL51 acts as a catalyst to accelerate cytoplasmic envelopment but that additional (redundant) cellular and/or viral mechanisms support envelopment in the absence of pUL51. Disruption of the pUL20-gK complex causes substantial defects in cytoplasmic envelopment and the cytoplasm of cells infected with HSV-1 ΔgK or ΔUL20 mutants has been shown to harbour a greater number of unenveloped membrane-associated capsids[17,47]. The gK/pUL20 complex has been shown to interact with pUL37, and TEM analysis revealed that unenveloped capsids accumulate in the cytoplasm if the interacting residues in pUL37 are mutated[91,92], suggesting that interactions between gK/pUL20 and pUL37 are required for the formation of virus assembly compartments. However, our study revealed that capsids still associate with membranes in the absence of gK, indicating an interaction of gK/pUL20 with pUL37 is not required for recruiting capsids to assembly compartment membranes (**Fig. 5–6**). What our CLXT data does demonstrate is that the activity of both gK and pUL51 (and by association the gK/pUL20 and pUL7/pUL51 complexes) are important for virion assembly to progress beyond

association of capsids with cytoplasmic membranes. Whether both these complexes function to regulate the similar cellular machinery involved in membrane curvature and/or scission events that are required to complete the cytoplasmic envelopment process, for example ESCRT activity, remains to be established. In addition to extensive membrane-associated cytoplasmic capsids being observed in ΔgK infected cells, linear arrays of unenveloped capsids were observed in the cytoplasm for this virus (**Fig. 6D**). Cytoplasmic capsids migrate along microtubules and these linear arrays could represent capsids stalled on microtubules when envelopment compartments become saturated with capsids in the absence of gK[64]. One surprising result was the observation of numerous stalled envelopment events in ΔgE infected cells, despite no defects in replication kinetics being observed for the ΔgE virus (**Fig. 8**). This could arise from subtle differences in the kinetics of envelopment, whereby a minor defect in ΔgE budding slows the rapid process of envelopment sufficiently for stalled budding profiles to be observed, but not for long enough to cause a significant defect in virus replication.

Previous ultrastructural analysis of HSV-1 has largely been performed using TEM, which retains some advantages over cryoSXT. TEM offers higher resolution, allowing different components of the virus assembly intermediates to be unambiguously identified, such as the capsid, tegument, and envelope, thereby negating the need for fluorescence correlation with genomically-encoded tags. This allows HSV strains lacking fluorescent fusion proteins to be imaged, reducing the risk that the fluorescent proteins attached to structural proteins could interfere with virus assembly. However, 2D cross-sections of cytoplasmic envelopment events visualised by TEM, which appear as a capsid encircled by a tubular C-shaped endomembrane, are compatible with more than one 3D model of envelopment; techniques such as cryoSXT that allow greater volumes of the cell to be imaged than TEM are required to clarify the envelopment mechanism. Our 3D CryoSXT analysis reveals numerous budding events occurring in spherical/ellipsoidal vesicles and fully enveloped virions within spherical/ellipsoidal carrier vesicles (**Fig. 7**). We therefore propose a model for HSV-1 envelopment wherein the apparently C-shaped endomembranes observed in TEM represent the cross-sectional appearance of a spherical or ellipsoidal vesicle deformed by budding of a capsid into the vesicle lumen (**Fig. 7**). We also observed several instances of polarised arrays of capsids around spherical vesicles for mutant viruses with delayed envelopment (ΔpUL11, ΔpUL51, ΔgK, and ΔgE) **(Fig. 8).** To the best of our knowledge such observations have not been made in TEM studies of HSV-1 assembly with wild type or mutant viruses. This discrepancy may result from the low probability of capturing multiple capsids bordering a vesicle within a single TEM ultrathin section. Our cryoSXT imaging shows a greater density of material on the side of the vesicle membrane nearer the capsid (**Fig. 8**), a feature that has also been observed in TEM[15]. One advantage of our CLXT imaging is the ability to extend such insights by revealing the enrichment of specific viral proteins (exemplified in our data by gM-mCherry) at the capsid-proximal pole of the vesicle. The observations are consistent with the hypothesis that HSV-1 budding is asymmetric, being initiated at a 'budding pole' that is rich in tegument and glycoproteins[65]. In the future, probes for different viral and host membrane proteins and specific lipid species in CLXT could shed light on membrane partitioning processes that occur during herpesvirus assembly.

An advantage of the relatively high-throughput analysis afforded by cryoSXT (compared to TEM and cryoET) is the ability to obtain robust particle size data *in cellulo*. No difference was observed in the measured width of nuclear capsids compared with membrane-proximal cytoplasmic capsids (**Fig. 9 and Table 1**), suggesting that there is only minimal recruitment of tegument around cytosolic capsids and/or that the tegument is too diffuse to produce detectable X-ray absorption. However, the average width of envelopment intermediates for ΔgE and ΔpUL51, where capsids are engaged with the membrane ('embedded'), is only approximately 32.7 nm lower than that of fully enveloped extracellular enveloped virions (**Fig. 9 and Table 1**). This suggests that that the tegument layer becomes compressed around capsids immediately prior to, or concomitantly with, virus budding.

In conclusion, our multi-modal imaging strategy has provided novel ultrastructural insight into HSV-1 assembly, allowing the assembly trajectory of wild-type and mutant viruses to be observed in 3D. This revealed that envelopment occurs by the lumenal budding of capsids at spherical/ellipsoidal vesicles, rather than by wrapping of tubular membranes around capsids, and that tegument compression is concomitant with budding. Polarised arrays of capsids at cytoplasmic vesicles were observed for several mutants, suggesting envelopment is focused to one side of the endomembrane, and CLXT imaging suggested that these capsid-proximal surfaces are enriched in viral glycoproteins. Previously uncharacterised defects in nuclear egress were observed for HSV-1 lacking VP16, pUL16 and pUL21. Furthermore, comparative analysis reveals that deletion of VP16, pUL11, gE, pUL51 or gK cause distinct defects in cytoplasmic envelopment. Our data highlight the contributions that key HSV-1 envelope and tegument proteins make to virus assembly and underscore the power of correlative fluorescence and X-ray tomography cryo-imaging for interrogating virus assembly.

Materials and Methods

Reagents

Quantifoil® 3 mm gold TEM grids with a holey carbon film (R 2/2, 200 mesh) were used as a substrate for cells prepared for cryopreservation. TEM grids were treated with poly-L-lysine (Sigma Aldrich). 150 nm gold fiducials were used to align cryoSXT projections (Creative Diagnostics Nanoparticle AF647).

Cell lines

U2OS cells (ATCC HTB-96; RRID CVCL_0042) and African green monkey kidney (Vero) cells (ATCC #CRL-1586) were cultured in Dulbecco's Modified Eagle's Medium (DMEM; Thermo Fisher Scientific) containing 10% (v/v) fetal bovine serum (FBS; Capricorn), 4mM L-glutamine (Thermo Fisher Scientific), and penicillin/streptomycin (10000 U/mL; Thermo Fisher Scientific). Hanks' Balanced Salt Solution (HBSS; Thermo Fisher Scientific) and 0.25% Trypsin-EDTA (Thermo Fisher Scientific) were used to

wash and detach adherent cells, respectively. Cells were maintained in a humidified 5% CO_2 atmosphere at 37°C.

Generation of mutants

Mutants were generated from a bacterial artificial chromosome carrying the KOS HSV strain[93]. A mutant was previously reconstituted from this system containing eYFP-VP26 and gM-mCherry[29]. This was used as the dfParental virus and the BAC from which it was derived was used as template for the mutagenesis of other mutants. A two-step red recombination system[94] was used to generate the mutants with the primers shown in **Supp. Table 1**. The ΔpUL11 virus was generated by introducing one stop codon at residue 3 of the UL11 open reading frame (ORF). The ΔpUL16 virus was generated by introducing three stop codons at residue 15 of the UL16 ORF. The ΔpUL21 virus was generated by introducing three stop codons at residue 23 of the UL21 ORF. The ΔUL34 virus was generated by deleting codons 1-228 from the UL34 ORF. The ΔVP16 virus was generated by deleting codons 1-478 from the UL48 ORF. The ΔpUL51 virus was generated by introducing three stop codons at residue 21 of the UL51 ORF. The ΔgK virus was generated by introducing three stop codons at residue 54 of the UL53 ORF. The ΔUS3 virus was generated by deletion of the entire coding sequence of US3. The ΔgE virus was generated by introducing three stop codons at residue 21 of the US8 ORF. Mutant BACs were transfected, together with a Cre recombinase expression plasmid (pGS403) to excise the BAC cassette from the KOS genome, into 6-well plates containing 70-80% confluent Vero cells to reconstitute the viruses, other than ΔUL34, ΔVP16, and ΔgK, which were transfected into the respective complementing Vero-modified cell lines: UL34CX, 16_8, and VK302[61,95,96]. Successive stocks were generated by infecting Vero cells or complementing cells at MOI = 0.01. Cells were harvested once all cells demonstrated cytopathic effect, freeze-thawed and sonicated at 50% amplitude for 40 seconds in a cuphorn sonicator. Final stocks were clarified by centrifugation at 3,200×g for 5 minutes in a benchtop centrifuge, divided into 10–20 µL aliquots and were stored at -70°C. All virus stocks were titrated on U2OS cells, Vero cells, or Vero-modified complementing cells.

Infection assays

For the immunoblots, Vero cells (**Fig. 1C–D**) and U2OS cells (**Supp. Fig. 7B**) were seeded in 6-well plates, were left to reach 70–80% confluency, were infected at MOI = 5 with indicated viruses in a minimal volume of medium (500 µL) and were incubated in a 5% CO_2, 37°C incubator. After 1 hour, the inoculum was diluted to 2 mL with fresh medium and cells were incubated overnight. For the single-step replication curves (**Fig. 2A**, **Supp. Fig. 2**, **and Supp. Fig. 7C**), U2OS cells were seeded in 24-well plates at a density of 1×10^5 cells per well and were infected the next day at MOI = 2 with the indicated viruses in a minimal volume of medium (250 µL) for 1 hour in a 5% CO_2, 37°C incubator. After 1 hour, the inoculum was aspirated off the cells and the cells were treated with citric acid solution (40 mM citric

acid pH 3, 135 mM NaCl, and 10 mM KCl) for 1 minute to inactivate unabsorbed virus. Citric acid solution was subsequently aspirated off the cells and the samples were washed thrice with 500 µL PBS before adding 500 µL fresh medium. For the plaque size assays (**Fig. 2B–C and Supp. Fig. 7D–E**), U2OS cells were seeded on 6-well plates, were left to reach ~90% confluency, and were infected with a low titer of the indicated viruses (calculated to produce an average of 30 plaques per well). Cells were incubated with reduced serum (2% v/v) medium supplemented with 0.3% high viscosity carboxymethyl cellulose and 0.3% low viscosity carboxymethyl cellulose for 72 hours. For cryoSIM and cryoSXT experiments (**Fig. 3–8 and Supp. Fig. 4–5**), TEM grids were treated by glow discharge and were incubated in filtered poly-L-lysine for 10 minutes in 6-well plates as described previously[26,54]. Poly-L-lysine was aspirated off and U2OS cells were seeded onto the holey-carbon coated side of the grids at a density of 3×10^5 cells per well. After overnight culture in a 5% CO_2 and 37°C incubator, the cells were infected at MOI = 2 with indicated viruses in a minimal volume of medium (500 µL) and were incubated in a 5% CO_2, 37°C incubator. After 1 hour, the inoculum was diluted to 2 mL with fresh medium and were incubated for an additional 14.5 hours. Samples were washed with twice with 1 mL serum-free medium and were then overlain with a staining solution containing 50 nM MitoTracker Deep Red (Thermo Fisher Scientific) in serum-free medium. For samples infected with the dfParental, ΔpUL16, ΔpUL21, ΔUL34, ΔVP16, and ΔUS3 viruses, the staining solution also contained 2 µg/mL Hoescht33342 (Thermo Fisher Scientific). Samples were washed twice with serum-free medium after 30 minutes of staining and the grids were loaded into a Leica EM GP2 plunge freezer set to 80% humidity. A working solution of gold fiducials was prepared by centrifugation of a 1 mL stock (provided in the *Reagents* section) at 12×g for 5 minutes at RT. The pellet was resuspended in HBSS and the working solution was sonicated at 80 kHz (100% power) and 6°C to disperse clumps of gold fiducials. A 2 µL solution of the working solution was overlain onto the holey-carbon coated side of the grids, which were then blotted for 0.5–1 seconds on the opposite side using Whatman paper. Grids were then immediately plunged into liquid nitrogen-cooled liquid ethane and were transferred into storage containers maintained under liquid nitrogen.

For immunoblots, infected cells were washed twice with 1 mL PBS, scraped off 6-well plates, and were centrifuged at 2000×g for 5 minutes. Pellets were isolated and lysed with a solution of Complete Protease Inhibitor without EDTA (Roche) diluted 1 in 10 in a lysis buffer (Sigma Aldrich) on ice for 20 minutes. Insoluble material was removed by centrifugation at 20,000×g, 4°C for 10 minutes. Supernatants were resuspended in SDS-PAGE loading buffer supplemented with 2-mercaptoethanol. To immunoblot pUL20 and gE, the mixtures were heated to 42°C for 20 minutes. To immunoblot the other proteins, separate mixtures were boiled in a water bath for 5 minutes. Samples were resolved on SDS-PAGE gels alongside a Blue Protein Standard Broad Range ladder (New England BioLabs). Bands were transferred onto nitrocellulose membranes and were blocked with a 5% (w/v) solution of milk powder in PBS. The following primary antibodies were used: anti-pUL11[59] at 1:1000, anti-pUL16[97] at 1:1000, anti-pUL21[33] at 1:1, anti-pUL34[98] at 1:500, anti-VP16[99] at 1:10, anti-pUL51 (3D3)[49] at 1:1,

anti-pUL20[47] at 1:1000, anti-pUS3[100] at 1:1000, anti-gE[101] at 1:10, anti-VP5[102] at 1:10, and anti-GAPDH at 1:1000 (GeneTex, GTX28245). Membranes were stained with the following secondary antibodies: IRDye 680T conjugated goat anti-rat (926–68029), donkey anti-rabbit (926–68023) or goat anti-mouse (926–68020), or LI-COR IRDye 800CW conjugated donkey anti-rabbit (926–32213), donkey anti-chicken (926–32218), or goat anti-mouse (926–32210). Primary and secondary antibody solutions were generated in PBS-T supplemented with 0.5% milk powder, membranes were washed 4 times for 5 minutes on a rocking platform with PBS-T after each round of antibody staining. For membranes immunoblotted for pUL16 or pUL21, TBS and TBS-T were used instead of PBS and PBS-T. An Odyssey CLx Imaging System (LI-COR) and Image Studio Lite Software (LI-COR) were used to visualise immunoblots.

Single-step replication curves

Infected samples were prepared as described in *Infection Assays* and were transferred to -70°C storage at 2, 6, 9, 12, and 24 hours post infection. After at least two hours of storage at -70°C, the samples were thawed at 37°C. This process of freeze-thawing was repeated and the thawed samples were scraped off the 24-well plates using the blunt end of a 1mL plunger and were transferred into 1.5 mL microcentrifuge tubes for -70°C storage for at least two hours. 10-fold serial dilutions of the samples were performed and titrated on Vero cells as previously described[49]. To logarithmically transform the PFU data, 0 values on the exponential scale were converted to 1.

Sequencing and alignment

Working stock solutions of ΔgK and dfParental HSV-1 were prepared for Sanger sequencing by adding 10 µL of virus stock to 200 µL of a Quantilyse solution[103]. Samples were heated to 55°C in a thermal cycler for 2.5 hours, 85°C for 45 minutes, and were left on hold at 10°C. 2 µL of these solutions were used as templates for PCR amplification with custom primers (**Supp. Table 2**). Amplicon products were purified (EconoSpin, Epoch Life Science) and analysed by Sanger Sequencing with custom sequencing primers (**Supp. Table 3**). The HSV-1 strain KOS UL53 sequence (encoding gK) was aligned with the sequencing results using Clustal Omega and were visualised using Jalview[104–106].

Plaque size assays

Infected cells were prepared as described in *Infection Assays* and were washed with 1 mL PBS at 72 hpi. Samples were fixed with 1 mL 4% formaldehyde for 10 minutes and were washed with 1 mL PBS. Samples were blocked for 30 minutes with a solution of 5% FBS and 0.1% Tween-20 in PBS on a rocking platform. Samples were incubated for 1 hour with a 1:10 dilution of anti-gD (LP2) in blocking buffer on a rocking platform[107]. Samples were washed with blocking buffer 3 times and were incubated

for 1 hour with a goat-derived anti-mouse IgG (H+L) secondary antibody conjugated to horseradish peroxidase (Thermo Fisher Scientific; product no. 31430) at 1:1000 in blocking buffer. Samples were washed with blocking buffer 3 times and once with PBS. Plaques were detected using either TrueBlue peroxidase substrate (Seracare) according to the manufacturer's instructions (**Supp. Fig. 7D–E**) or with ImmPACT DAB peroxidase substrate (Vector SK105) according to the manufacturer's instructions (**Supp. Fig. 3**). Images were captured using an EPSON scanner V600 at 1200 dpi. Plaque area (in pixels) was measured using Fiji by applying an intensity threshold to images of each plaque, creating binary masks with a value of 0 for background and 1 for plaque pixels[108,109]. Plaque area was determined by automated counting of each pixel within a plaque.

CryoSIM

Cryopreserved TEM grids were placed onto a liquid nitrogen cryostage (Linkam) and were imaged by cryoSIM as previously described[56]. The cryoSIM was developed in-house as previously described[110]. Hoescht stain fluorescence was excited using a 405 nm laser and was detected using an EM-452-45 filter (452 ± 22.5 nm). eYFP-VP26 fluorescence was excited using a 488 nm laser and was detected using an EM-525-50 filter (525 ± 25 nm). gM-mCherry fluorescence was excited using a 561 nm laser and was detected using an EM-605-70 filter (605 ± 35 nm). MitoTracker Deep Red fluorescence was excited using a 647 nm laser and was detected using an EM-655-lp filter (≥ 655 nm). SIM data were reconstructed using SoftWoRx (AppliedPrecision Inc., Issaquah, WA) and the fluorescent channels were aligned using Chromagnon[111].

CryoSXT

Cryopreserved TEM grids were loaded into a liquid nitrogen-cooled vacuum chamber of an UltraXRM-S/L220c X-ray microscope (Carl Zeiss X-Ray Microscopy) at beamline B24 of the Diamond Light Source[66]. Incident soft X-rays generated at the synchrotron (500 eV, λ = 2.48 nm) were used to illuminate the samples and transmitted X-rays were detected using a 1024B Pixis CCD camera (Princeton Instruments). Transmitted light was focused using a 25 nm zone plate objective with a nominal resolution limit of 25 nm. Samples were focused by Z translations of the zone plate and samples were centred along a rotational axis by Z translations of the sample grid. Individual X-ray projections (9.46×9.46 µm) were captured and tiled together in 7×7 montages known as X-ray mosaics to inspect sample quality and identify regions of interest for tomography. Tomographic data were collected at fields of view measuring 9.46×9.46 µm. In each case, a collection of X-ray projections known as a tilt series were acquired by rotating the sample with maximum tilt angles of –60°/+60° and acquiring images at increments of 0.2° or 0.5°. A 0.5 or 1 second exposure time was used depending on the intensity of the transmitted X-rays. Tilt series were reconstructed using IMOD (version 4.9.2)[112] as previously described[26].

Correlation of cryoSIM and cryoSXT

CryoSIM data was correlated onto CryoSXT data using easyCLEMv0[113] as previously described[114] with a few differences. CryoSXT tomograms were used as the target for the correlation and a frame was added around the tomogram, increasing the XY dimensions to 1200×1200 voxels. This increased the canvas size of the transformed cryoSIM data and reduced the probability that edges of the cryoSIM data would overlap with the tomogram at the centre of the frame during XY translations and rotations of the cryoSIM data. To avoid the need for an affine transformation model, maximum Z projections of cryoSIM data were used to generate transformation files using the rigid transformation model. The X-ray mosaic and a minimum Z projection of the tomogram were used as targets for these transformations. Rigid-transformation files generated using the 2D maximum Z projections of the cryoSIM data were applied to the 3D Z stacks to prevent the anisotropic stretching of signal generated by affine transformations in lieu of rotation around the X or Y axis. Before conducting a 3D rigid transformation of cryoSIM Z stacks onto the target tomogram, the number of slices in the cryoSIM image was increased 5-fold (reducing the voxel depth from 125 nm to 25 nm). This made it easier to correlate the front and back edges of mitochondrial fluorescence and tomographic mitochondria together. The TransformJ plugin in Fiji was used to further fine-tune the correlation where needed[109].

Quantitation of nuclear egress

3D CryoSIM images were collected from TEM grids containing U2OS cells infected at MOI = 2 with mutants as described in *Infection Assays*. A Hoechst 33342 stain was used to label the nucleus. Reconstructed images of eYFP-VP26, gM-mCherry, and Hoescht stain were registered together and maximum intensity projections in Z were generated using Fiji. Edges of the nucleus and plasma membranes were delineated using the Hoescht and gM-mCherry fluorescence, respectively, to determine nuclear and cytoplasmic regions of interest. Cells infected with the ΔgE virus were used as a negative control for attenuation in nuclear egress. As these cells did not contain a Hoescht stain, the borders of the nuclei in the X-ray mosaics were used to demarcate the nuclei in the fluorescence. A threshold was applied to the eYFP-VP26 maximum projection to filter out background and isolate pixels containing capsid fluorescence. The ratio of eYFP-VP26^{+} pixels was measured between the nuclear and cytoplasmic regions of interest. A total of 95 infected cells were included in the analysis. Infected cells were included in the analysis if the JAC (determined by a concentration of gM-mCherry vesicles) was not located over or under the nucleus with respect to the XY plane. Exclusion criteria included cells with indistinguishable boundaries from each other, cells with a faint Hoescht nuclear stain, or cells that had a majority of their area located outside the field of view.

Quantitation of cytoplasmic clustering

3D CryoSIM images were collected from TEM grids containing U2OS cells infected at MOI = 2 with mutants as described in *Infection Assays*. Reconstructed images of eYFP-VP26 and gM-mCherry were registered together using Chromagnon[111]. Borders of the JAC were determined based on the relative intensity of the gM-mCherry fluorescence. Binary masks of eYFP-VP26 and gM-mCherry fluorescence were generated by applying thresholds that filter out background and noise. The total number of retained pixels in the borders of the JAC were counted for the two channels and an eYFP-VP26 / gM-mCherry ratio was produced. In order to calculate colocalization between these channels, a spatial coincidence-based method known as Manders correlation was used instead of intensity-based methods, such as Pearson's correlation, to minimize the influence of noise, background, and cryoSIM reconstruction artefacts. Thresholds on intensity were applied to the eYFP-VP26 and gM-mCherry fluorescent channels using Fiji, and the number of fluorescent pixels were quantitated from masks[108,109]. Overlap between the channels was determined using the subtract function in Fiji. To calculate M1 values, masks of gM-mCherry fluorescence were subtracted from eYFP-VP26 masks, and the remaining pixels were quantitated and subtracted from the total pixels in the eYFP-VP26 mask to determine the number of eYFP-VP26 pixels that overlapped with gM-mCherry. M1 values were calculated in Excel (Microsoft) by dividing the number of overlapping pixels by the total number of eYFP-VP26 pixels in the region of interest. To calculate M2 values, the same process was performed but with the two channels switched. Exclusion criteria included cells where the JAC overlapped with the nucleus or cells where the JAC was partially excluded from the field of view.

Quantitation of membrane intensity

The membrane intensity of vesicles surrounded by capsid arrays was measured from signed 16-bit tomograms generated by WBP without reducing noise by applying a SIRT-like filter. The minimum voxel intensity was measured from 3×3 voxel matrices at 30 points around the vesicle. Data were collected from 3 tandem projection planes spanning 30 nm in depth using the same 30 XY coordinates and the mean ± SD were graphed (**Fig. 8E–F** and **Supp. Fig. 7B**). Of the 30 coordinates assessed, those nearest to proximal capsids were marked and this was used to draw a boundary between capsid-proximal and capsid-distal sides of the vesicle.

Segmentation

Segmented volumes were generated manually using Segmentation Editor in Fiji[109]. The X-ray absorbance heatmap (**Fig. 8G–H**) was generated by applying the Fire lookup table to the tomogram in Fiji and superimposing it onto the segmented volume of the vesicles[109]. Segmented volumes were rendered in 3D using 3D Viewer in Fiji[109]. Segmented vesicles (**Fig. 7B–C, Fig. 8A–D, I** and **Supp. Fig. 7A**) appeared open-ended at the anterior and posterior faces with respect to the imaging plane because cryoSXT produced less contrast in those regions compared with side regions perpendicular to the imaging plane, making it impossible to fully segment the vesicles without extrapolation. This contrast

discrepancy was not due to a limitation in the tomogram's depth as cryoSXT captured the entire volume of cells within each field of view but was due to a mechanical constraint in the X-ray microscope. During tilt series collection, the sample could only be rotated by a 120° range (–60° to +60°) rather than a desired 180° range (–90° to +90°) to avoid collisions with other components in the microscope. During acquisition, the vesicle's side regions were positioned parallel with the X-ray beam at 0°, maximising X-ray absorption and contrast. As the anterior and posterior faces perpendicular to the side regions were never positioned at ±90°, they were never parallel with the X-ray beam, reducing absorption and contrast in those regions. The open ends all share the same orientation, confirming that they are artefacts of the imaging setup rather than *bona fide* features.

Graphs and statistics

Single-step replication curves (**Fig. 2A, Supp. Fig. 2, and Supp. Fig. 7**) and graphs of membrane intensity (**Fig. 7E–F and Supp. Fig. 7B**) were generated in Excel (Microsoft). Relative plaque area graphs (**Fig.2B and Supp. Fig. 7E**), the nuclear/cytoplasmic capsid ratio graph (**Fig. 4B**), the eYFP-VP26/gM-mChery ratio graph (**Fig. 5D**), the Manders correlation graphs (**Fig. 5E and Supp. Fig. 4**) and the graph showing the width of virus particle intermediates (**Fig. 9**) were generated using the ggplot2 package[115] in R studio[116]. The graph showing the width of vesicles surrounded by capsid arrays was generated using SuperPlots[117] (**Supp. Fig. 6C**). Single-step replication curves report the mean Log_{10}(PFU) values from two technical repeats and the error bars indicate range. For the graphs of membrane intensity for which the data was normally-distributed, a two-tailed t-test was used to assess the significance of differences between voxel intensity between the capsid-proximal and capsid-distal sides of the vesicle (**Fig. 8E–F and Supp. Fig. 7E**). Mann-Whitney *U* tests were used to assess significant differences for non-normally distributed data (**Fig. 4B, Fig. 5D–E, Fig. 9, Fig. 2B, Supp. Fig. 4, and Supp. Fig. 7E**). The boundary was determined by the location of the capsids. The width of vesicles surrounded by capsid arrays was measured using *Contour*[68].

Acknowledgements

We thank Diamond Light Source for access to beamline B24 (proposals MX18925, MX19958, BI21485, BI23508, BI25247, BI26657 and BI30442) and the experimental hall coordinators for helpful support. We thank members of beamline B24 at the Diamond Light Source (Thomas Fish, Archana Jadhav, Mohamed Koronfel, Ilias Kounatidis, Chidinma Okolo, Matt Spink, and Nina Vyas) for technical support with cryoSXT and cryoSIM. We thank the DNA Sequencing Facility at the Department of Biochemistry, University of Cambridge for their support. We thank Mike Hollinshead (University of Cambridge) for assistance with electron microscopy of HSV-1 infection. This work was supported by a PhD studentship co-funded by Diamond Light Source and the Department of Pathology, University of Cambridge, to KLN, by a Sir Henry Dale Fellowship, jointly funded by the Wellcome Trust and the Royal Society

(098406/Z/12/B) to SCG, and by a Biotechnology and Biological Sciences Research Council (BBSRC) Research Grant (BB/M021424/1) to CMC. For the purpose of Open Access, the authors have applied a CC BY public copyright licence to any Author Accepted Manuscript (AAM) version arising from this submission.

Data availability

Original imaging data for tomograms illustrated in the manuscript will be deposited in the University of Cambridge Apollo Repository and representative tomograms will be published in the EMPIAR repository (EMBL-EBI) upon acceptance.

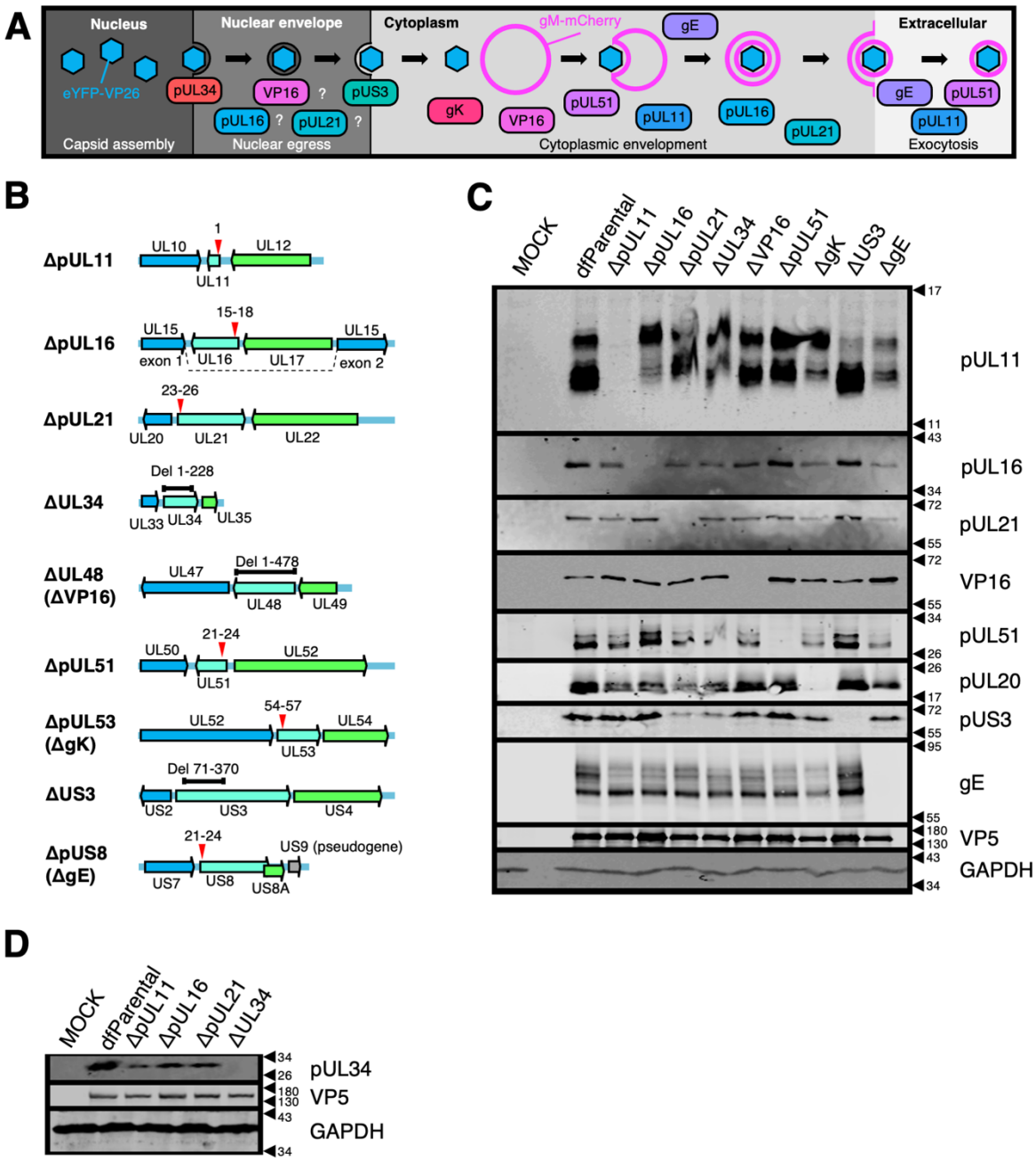

Figure 1. Characterisation of HSV-1 mutants. (**A**) Schematic of HSV-1 assembly with the proposed roles of viral proteins at different stages. Question marks denote that the role of the corresponding protein at that stage of HSV-1 assembly remains uncertain. Mutants with stop codons are named Δ + protein name (e.g. ΔpUL11) whereas mutants with sequence deletions are named Δ + gene name (e.g. ΔUL34). Unique long (UL) and unique short (US) names are used except for proteins more commonly known by another name (i.e. ΔVP16, ΔgK, and ΔgE). (**B**) Schematic of recombinant viruses generated. Deletions (black bars) or stop codons (red arrows) were introduced into genes of interest (cyan) to prevent protein expression. Numbering refers to the amino acid residues of the corresponding protein. Flanking genes (blue and green) and pseudogene (mutated US9; grey)[118] in HSV-1 strain KOS are indicated. (**C-D**) Absence of protein expression was confirmed by immunoblotting infected Vero cell

lysates with VP5 and GAPDH as viral and cellular loading controls, respectively. Due to unavailability of an antibody that recognises gK, immunoblotting of pUL20 was used as an indicator of loss of gK expression since stable expression of gK and pUL20 relies on the presence of each other[119].

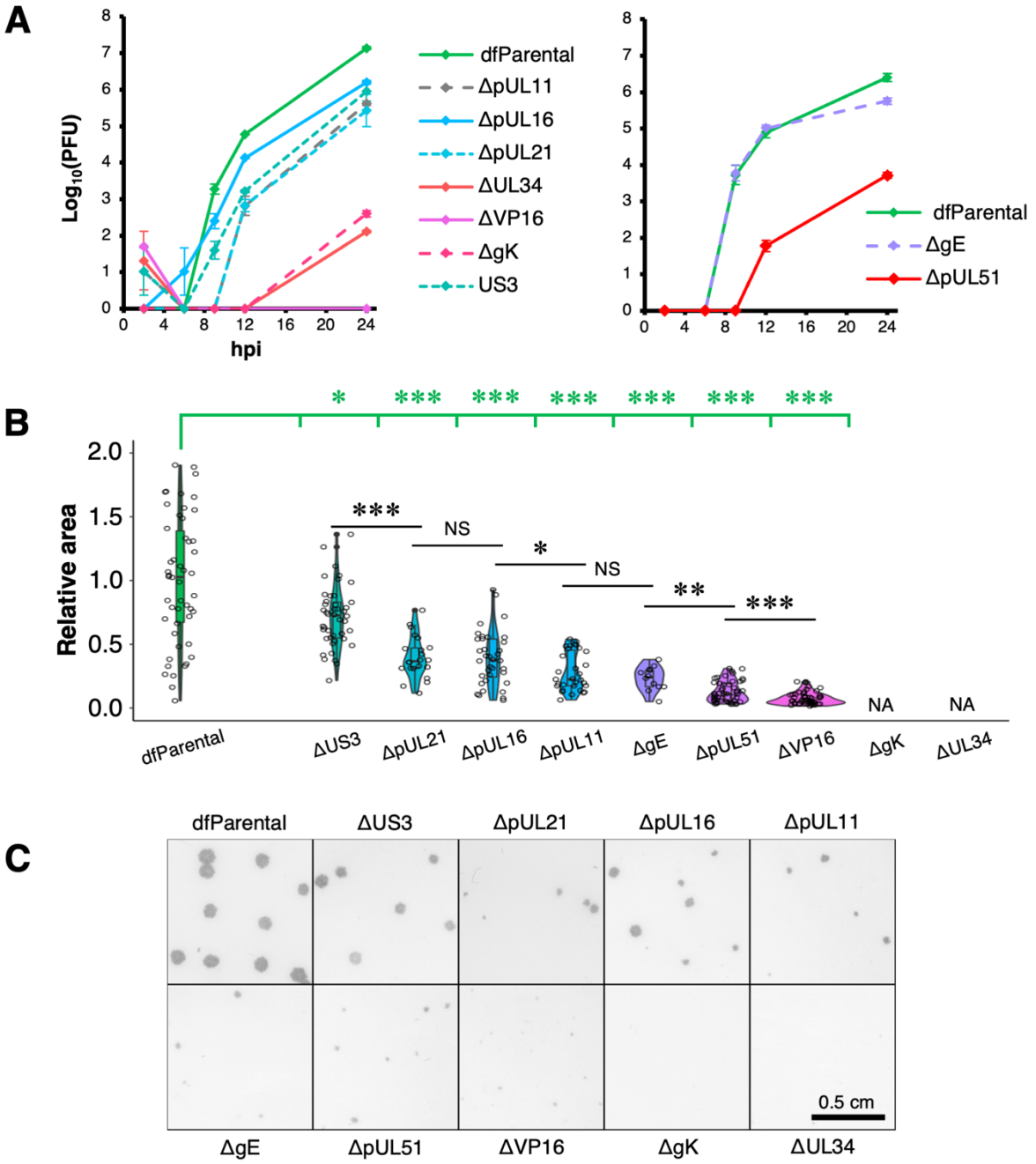

Figure 2. Replication kinetics and plaque assays of HSV-1 mutants. (**A**) Single-step replication curves on U2OS cells infected at MOI = 2 with virus. dfParental refers to eYFP-VP26 & gM-mCherry KOS used as a parental strain. U2OS cells were infected at MOI = 2 with virus over a 24 h period and were treated with citric acid at the 1-hour timepoint to deactivate residual input virus. Titrations were performed on parental or complementing Vero cells. Two technical repeats were measured for each timepoint, and the data are representative of two biological replicates (**Supp. Fig. 2**). Error bars show mean ± range. (**B**) 72-hour plaques were immunostained for gD using an antibody conjugated to horseradish peroxidase and were subsequently stained with DAB. Plaque area (pixels) were measured by applying thresholds to intensity using Fiji and quantifying the number of pixels in each plaque from binary masks[108,109]. Given the skewed distributions, non-parametric Mann-Whitney *U* tests were used

to assess the significance of differences. P-value thresholds: <0.05 (*), <0.005 (**), and <0.0005 (***). NS, no significance; NA, not applicable. (**C**) Images of 72-hour plaques from dfParental and mutants.

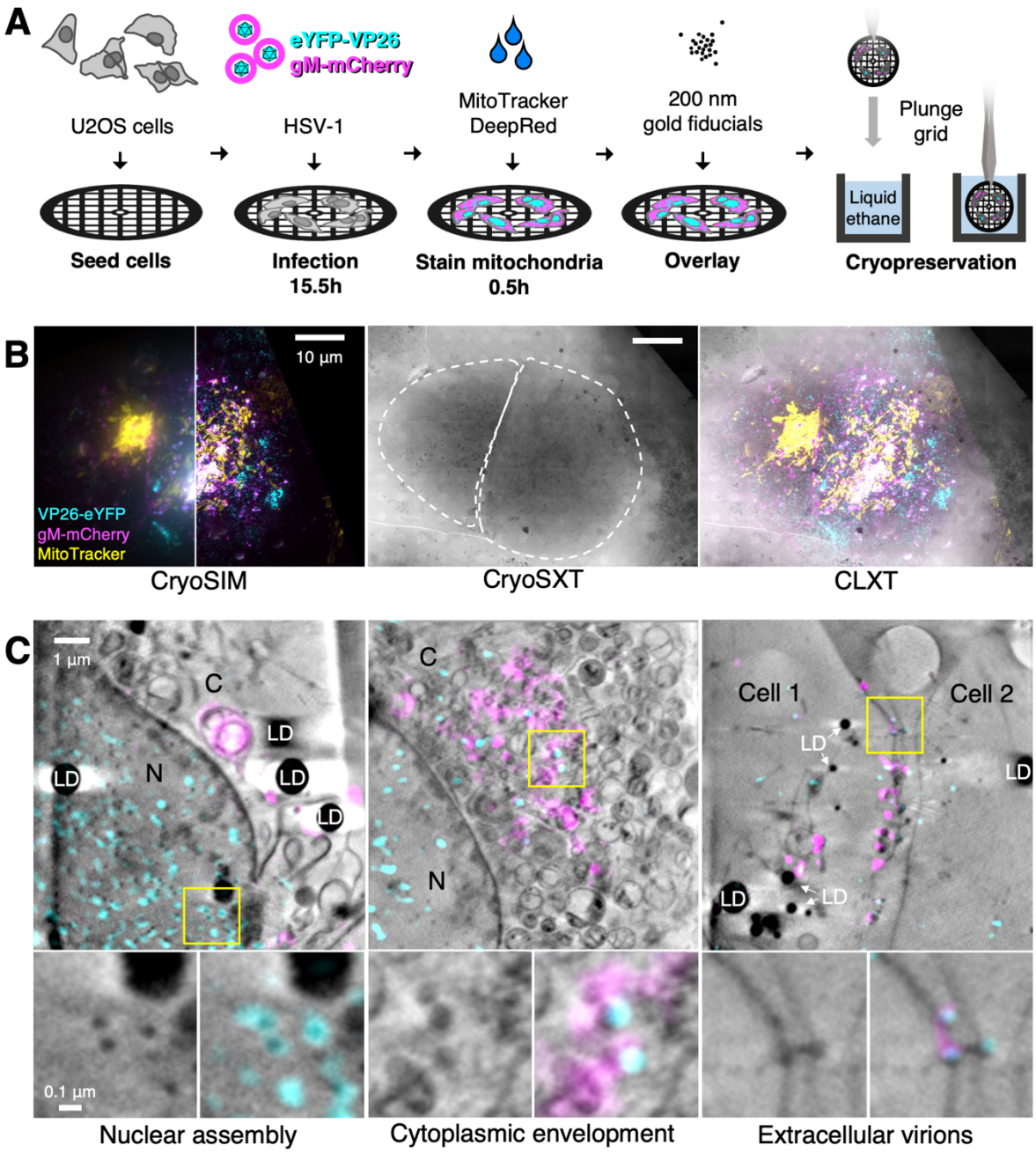

Figure 3. Correlative imaging workflow to study dfParental HSV-1 assembly. U2OS cells were infected at MOI = 2 with dfParental HSV-1 for 16 hours. (**A**) A schematic of sample preparation. U2OS cells were seeded on 3 mm TEM grids, infected with the dfParental virus for 15.5 hours, mitochondria were stained with MitoTracker™ Deep Red (Thermo Fisher Scientific) for 0.5 hours, and 200 nm gold fiducials were overlayed onto the cells immediately before cryopreservation by plunge cryocooling in liquid ethane. (**B**) Cryopreserved samples were imaged first by cryoSIM and subsequently by cryoSXT. The left and right side of the cryoSIM image shows the data at conventional resolution (left) and after it was super resolved in a cryoSIM reconstruction (right). CryoSIM fluorescence was then correlated onto the CryoSXT datasets by comparing the MitoTracker stain with mitochondria in the tomograms. Scale bars = 10 µm. (**C**) CLXT was used to identify virus assembly intermediates in U2OS cells infected with

1 the dfParental tagged virus. eYFP-VP26^{+}/gM-mCherry^{-} particles were identified in the nucleus (N).
2 eYFP-VP26^{+}/gM-mCherry^{+} particles were identified in the cytoplasm (C) where cytoplasmic
3 envelopment occurs. eYFP-VP26^{+}/gM-mCherry^{+} particles were also identified in spaces between cells.
4 LD = lipid droplets.
5

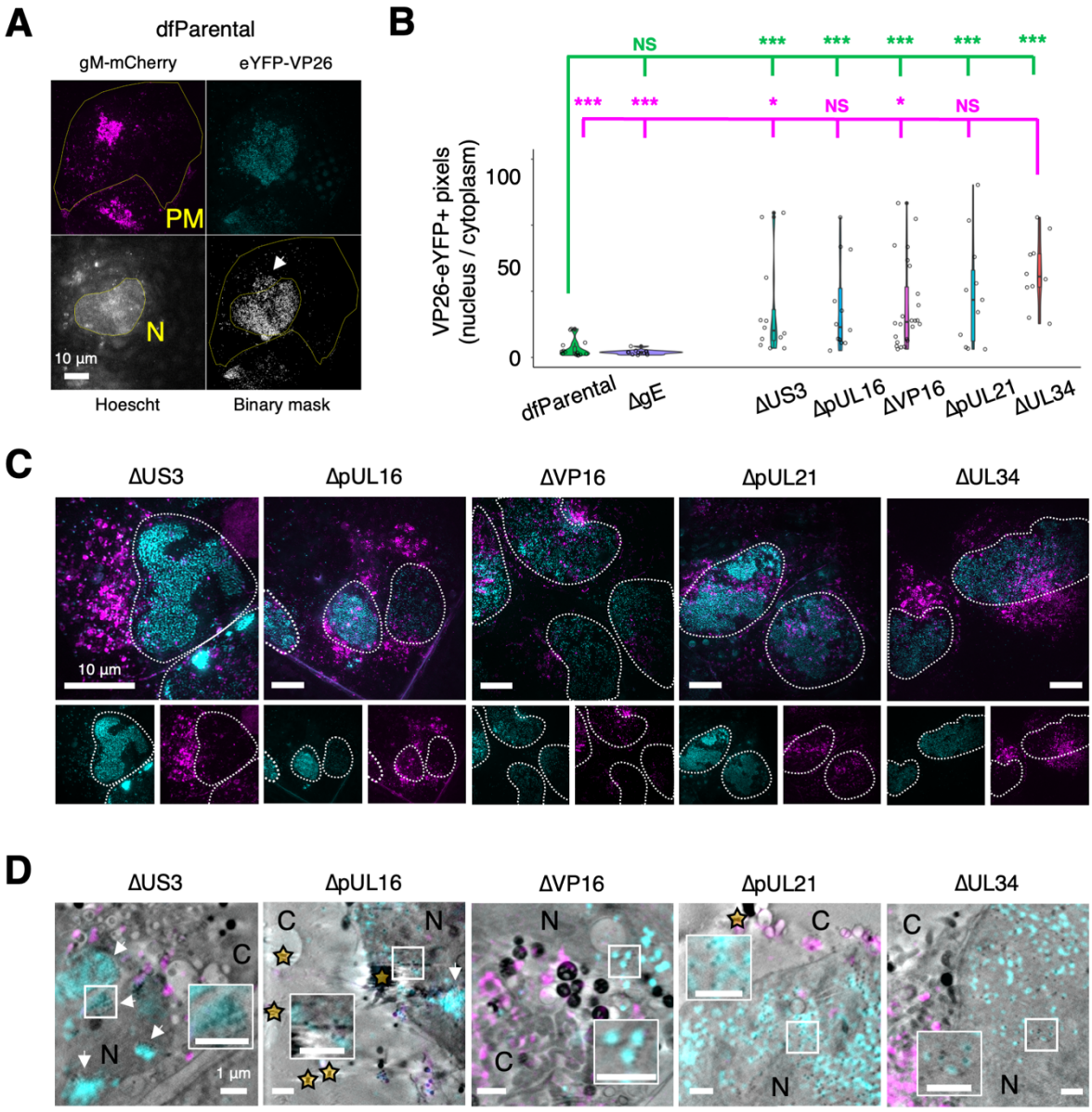

Figure 4. CryoSIM and CLXT of nuclear egress attenuation. U2OS cells were infected at MOI = 2 with indicated viruses for 16 hours. Mutant-specific defects in nuclear egress were investigated using maximum Z projections of cryoSIM data. (**A**) eYFP-VP26 fluorescence was captured in punctate form, representing individual virus particles or clusters. Digitally saturated gM-mCherry was used to delineate the plasma membrane (PM) of infected cells and the Hoechst stain was used to delineate the nucleus (N). A binary mask of eYFP-VP26 fluorescence was generated to include capsids or capsid clusters and filter out background or noise. The arrow indicates fluorescent viral proteins in the cytoplasm. Scale bar = 10µm. (**B**) The number of pixels containing capsids or capsid clusters in the nucleus and cytoplasm was counted using the plasma membrane and nucleus borders. The nuclear:cytoplasmic (N:C) ratio of capsids was lowest for the dfParental-infected cells and the ΔgE-infected cells (negative

control) and was significantly higher for the other mutants. Owing to the skewed distributions, the significance of differences was assessed using non-parametric Mann-Whitney *U* tests between dfParental (N=14) (green statistics) or ΔUL34 (N=10) (pink statistics) and other viruses, specifically ΔpUL16 (N=13), ΔpUL21 (N=11), ΔUS3 (N=13), ΔVP16 (N=24), and ΔgE (N=12). NS; no significance. P-value thresholds: <0.05 (*), <0.005 (**), and <0.0005 (***). (**C**) Representative viral fluorescence cryoSIM data for the mutants. Scale bars = 10µm. (**D**) Correlative cryoSIM and cryoSXT data for the mutants. Inset images show correlated nuclear capsids at twice the magnification. Scale bars = 1µm. Nuclear clusters of capsids (known as assemblons[120,121]) are visible in the ΔUS3 and ΔpUL16 datasets (arrows). Stars indicate gold fiducials. C, cytoplasm.

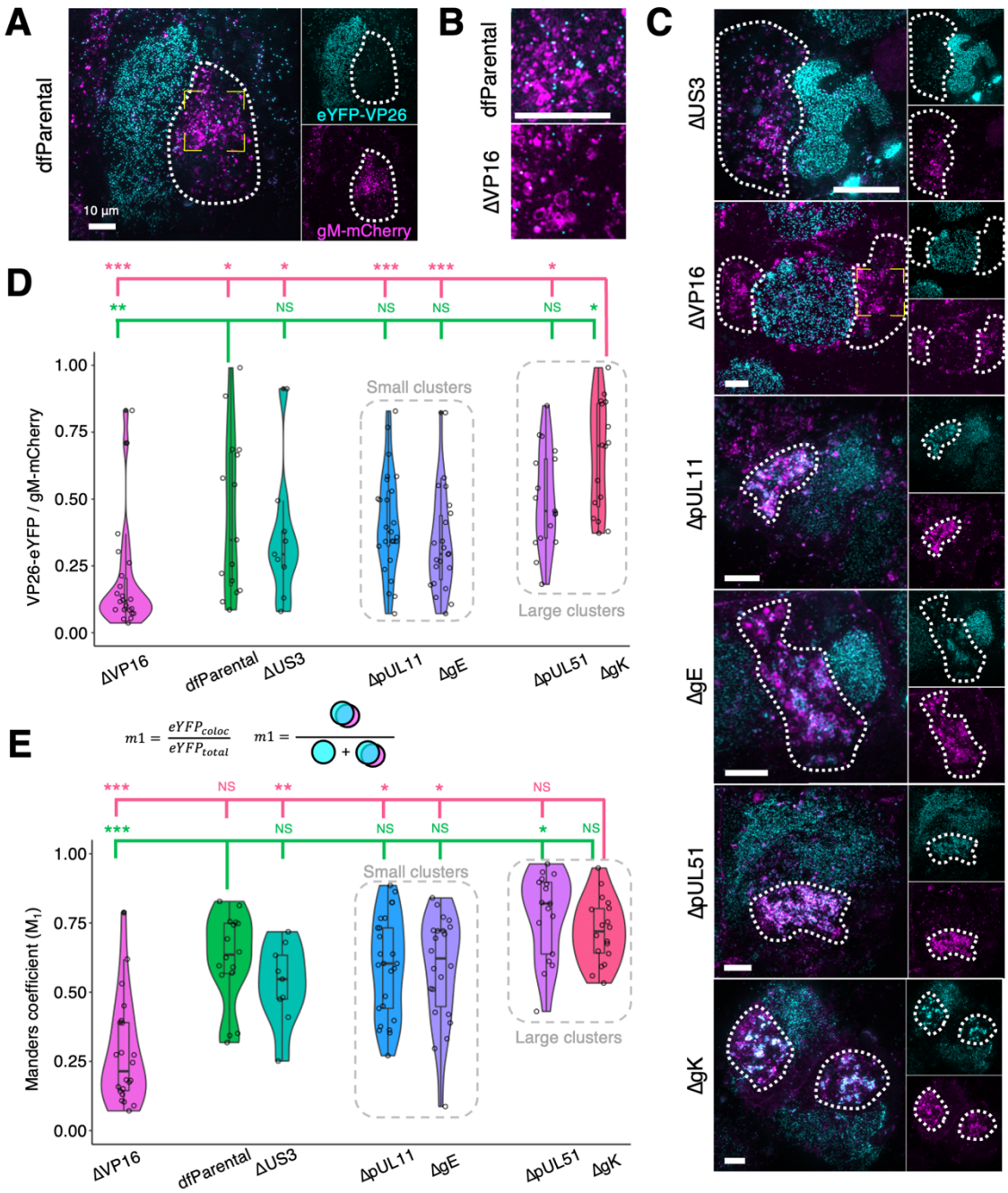

Figure 5. Cytoplasmic clustering of virus particles imaged using cryoSIM. U2OS cells were infected at MOI = 2 with indicated viruses for 16 hours. Cytoplasmic clustering of mutants was investigated using maximum Z projections of cryoSIM data. Scale bars = 10 µm. (**A**) gM-mCherry fluorescence was used to determine the cytoplasmic region in which virus assembly occurs, known as the juxtanuclear assembly compartment (JAC, dotted outline). The yellow corner markings denote the region of the dfParental virus-infected cell shown in B. (**B**) Cytoplasmic capsids at the JAC in ΔVP16-infected cells were less abundant and less closely associated with gM-mCherry+ endomembranes compared with those of dfParental-infected cells. (**C**) Representative images of JACs (dotted outline) for mutants. The JACs for the ΔUS3 virus were similar to those of the dfParental. ΔVP16 produced few cytoplasmic virus particles, ΔpUL11 and ΔgE produced small cytoplasmic clusters of capsids, and

ΔpUL51 and ΔgK produced large cytoplasmic capsid clusters. The yellow corner markings denote the region of the ΔVP16 virus-infected cell shown in B. (**D**) Thresholding of eYFP-VP26 and gM-mCherry fluorescence to filter out noise and background was performed and binary masks were produced. The ratio of eYFP-VP26^{+} pixels to gM-mCherry^{+} pixels at the JACs was reported. Data from the ΔUS3 virus were included as negative control for attenuation in cytoplasmic virion assembly. (**E**) Manders coefficients (M_1) were measured for each virus and represent the amount of eYFP-VP26 fluorescence that colocalise with gM-mCherry ($eYFP_{coloc}$) as a proportion of all eYFP-VP26 fluorescence at the JAC ($eYFP_{total}$). M_1 values were markedly lower for the ΔVP16 virus than other viruses. M_2 values are shown in **Supp. Fig. 4**. Mann-Whitney *U* tests were performed to assess significance of differences between dfParental (N=16) (green statistics) or ΔgK (N=18) (pink statistics) and other viruses, specifically ΔUS3 (N=9), ΔVP16 (N=22), ΔgE (N=23), ΔpUL11 (N=25), and ΔpUL51 (N=17). P-value thresholds: <0.05 (*), <0.005 (**), and <0.0005 (***). NS, no significance.

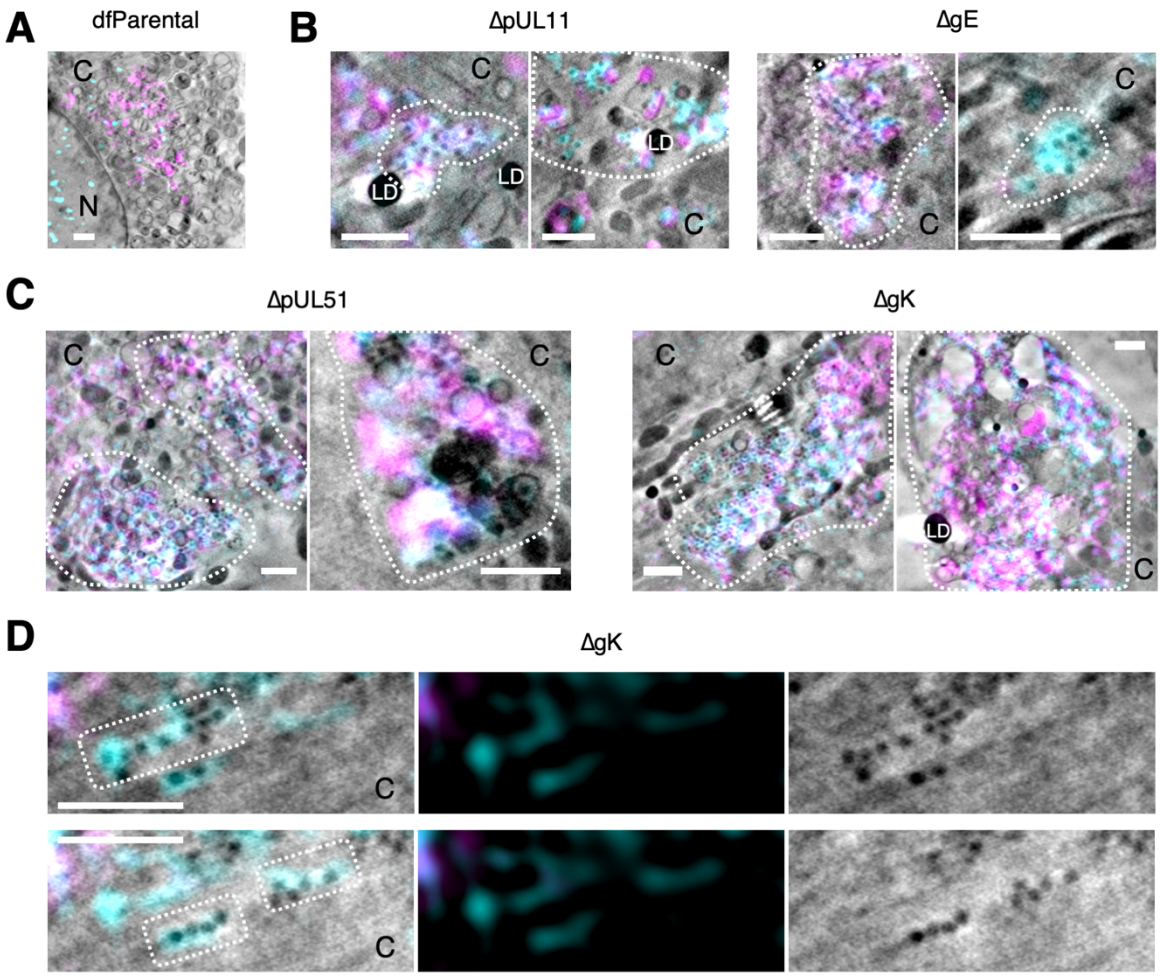

Figure 6. CLXT of cytoplasmic clusters of mutants. U2OS cells were infected at MOI = 2 with indicated viruses for 16 hours. (**A**) Individual envelopment events (arrows) as opposed to cytoplasmic clusters were observed for the dfParental virus. To aid visual comparison, this panel depicts the same data as shown in **Fig. 3C**. C, cytoplasm; N, nucleus. (**B**) Cells infected with ΔpUL11 or ΔgE viruses contained small clusters of capsids (outlined) in the JACs. (**C**) Cells infected with ΔpUL51 or ΔgK viruses contained large clusters of capsids (outlined) in the JACs. (**D**) Linear arrays of eYFP-VP26^{+}/gM-mCherry^{-} virus particles (outlined) were observed in the cytoplasm of cells infected with ΔgK. Scale bars = 1 µm.

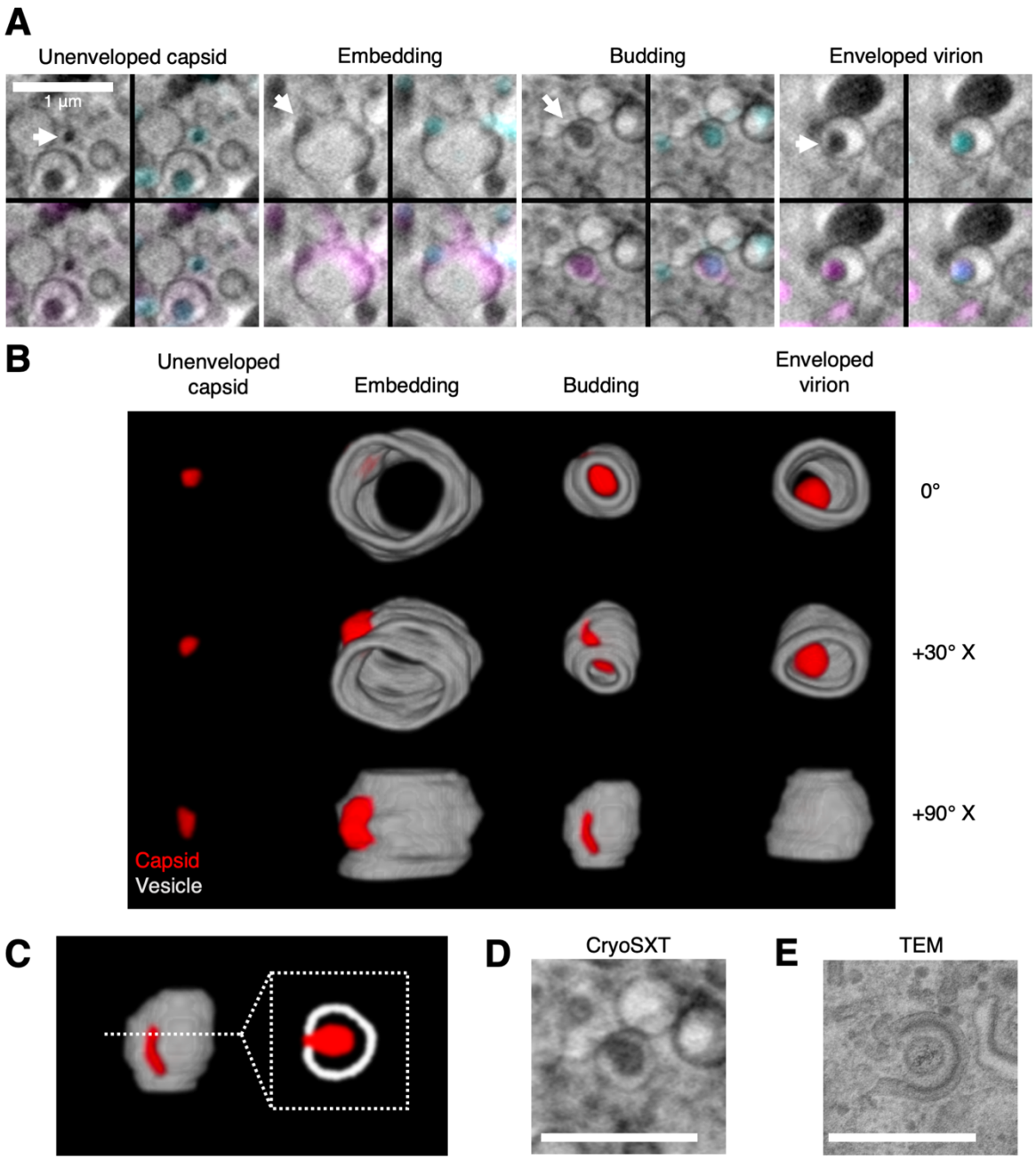

Figure 7. 3D Snapshots of the trajectory of ΔpUL51 HSV-1 envelopment within the cytoplasm. U2OS cells were infected at MOI = 2 with ΔpUL51 HSV-1 for 16 hours. (**A**) CLXT revealed multiple stages in the assembly of the ΔpUL51 virus (arrows). (**B**) 3D renderings of the assembly stages captured by CLXT in A at different rotations around the X axis. The vesicles appear open-ended because the anterior and posterior faces lack sufficient contrast for reliable segmentation — a result of the X-ray tilt series spanning 120° rather than 180°. (**C**) Capsids can be seen budding into vesicles. A cross section through the middle gives the appearance of a capsid being wrapped by a tubular membrane. (**D**) A 2D CryoSXT projection of an envelopment event. (**E**) A 2D TEM of an envelopment event from an HFF-hTERT cell infected with an untagged WT HSV-1 (KOS strain). Scale bars = 1 µm.

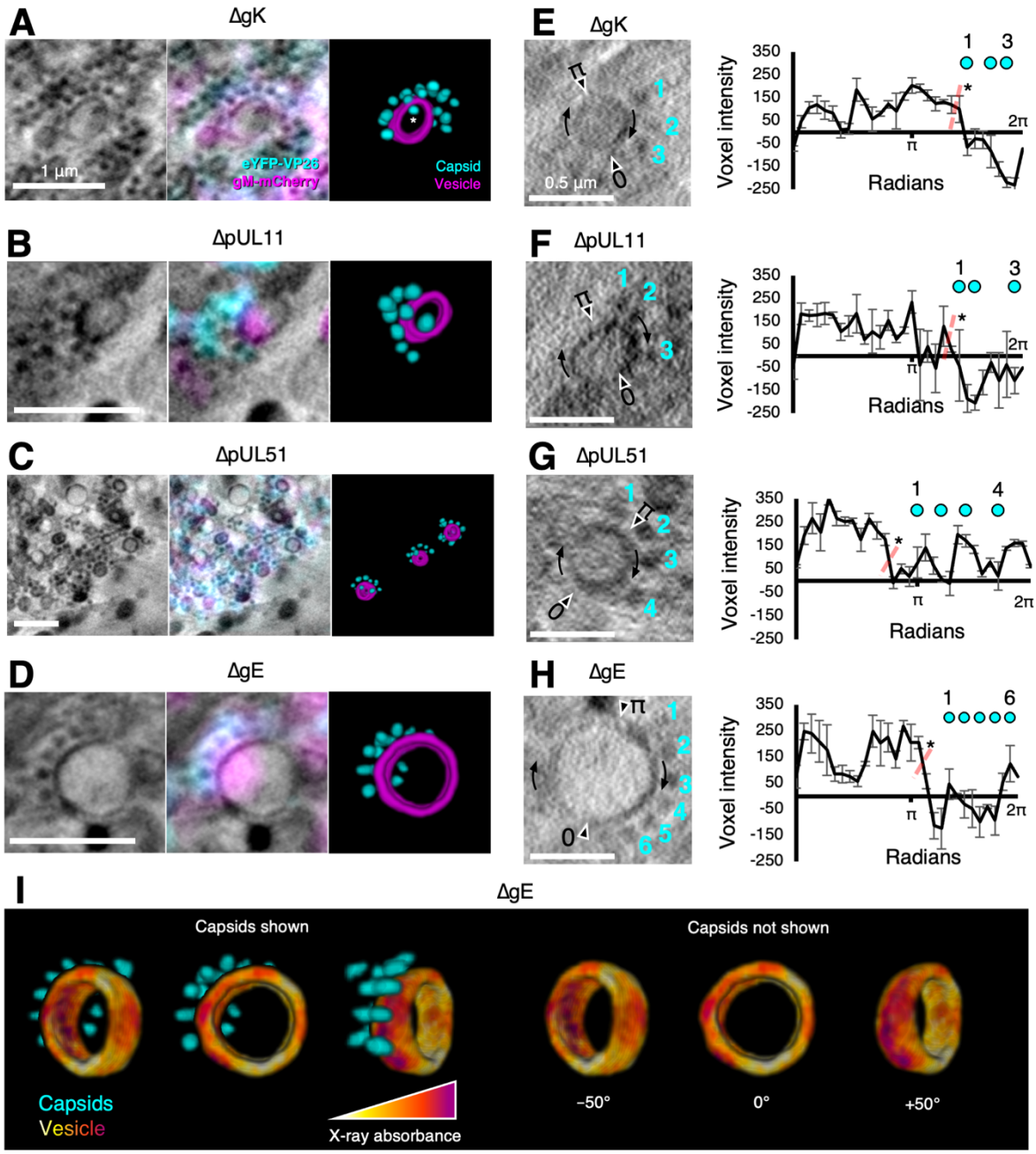

Figure 8. Mutants exhibit features of stalled envelopment. U2OS cells were infected at MOI = 2 with indicated viruses for 16 hours. (**A–D**) Arrays of unenveloped cytosolic capsids were observed near gM-mCherry enriched vesicles for the indicated viruses. Vesicles were enriched in gM-mCherry at the pole nearest the capsid arrays. We interpret these features as capsids interacting with the appropriate target membranes but experiencing a delay or defect in budding. Some capsids appear to be located in the lumen of the vesicle (e.g. capsid marked with an asterisk (*) in **A**), but these are in fact external and located in front of or behind the open-ended segmentation of the vesicle. The vesicles appear open-ended because the X-ray tilt series spanned only 120°, causing the anterior and posterior faces to lack sufficient contrast for reliable segmentation. (**E–H**) For each indicated virus, the voxel intensity was measured at 30 points on the vesicles to provide a measure of the X-ray absorbing material present on

the vesicle. Voxel intensities were plotted against the positions of the proximal capsids. Voxel intensities were measured from 3 projection planes spanning a depth of 30 nm and error bars show mean ± SD of these 3 planes. Two-tailed t-tests were performed to determine a significance of difference between the side of the vesicle nearest the capsids and the other side as indicated by the dotted red line. Voxel intensity was lower on the side nearest the capsids, indicating this pole of the membrane contained a greater X-ray absorbing material. (**I**) A falsecoloured heatmap of voxel intensity from the cryoSXT data was superimposed onto the vesicle segmentation from D. The vesicle is displayed at three angles with or without the proximal capsid arrays. The reciprocal of voxel intensity was used a proxy for X-ray absorbance. The pole of the vesicle near to the capsid arrays had greater X-ray absorption (red/purple) than the opposite pole (yellow/orange). Scale bars = 1 µm in **A–D** and 0.5 µm in **E–H**.

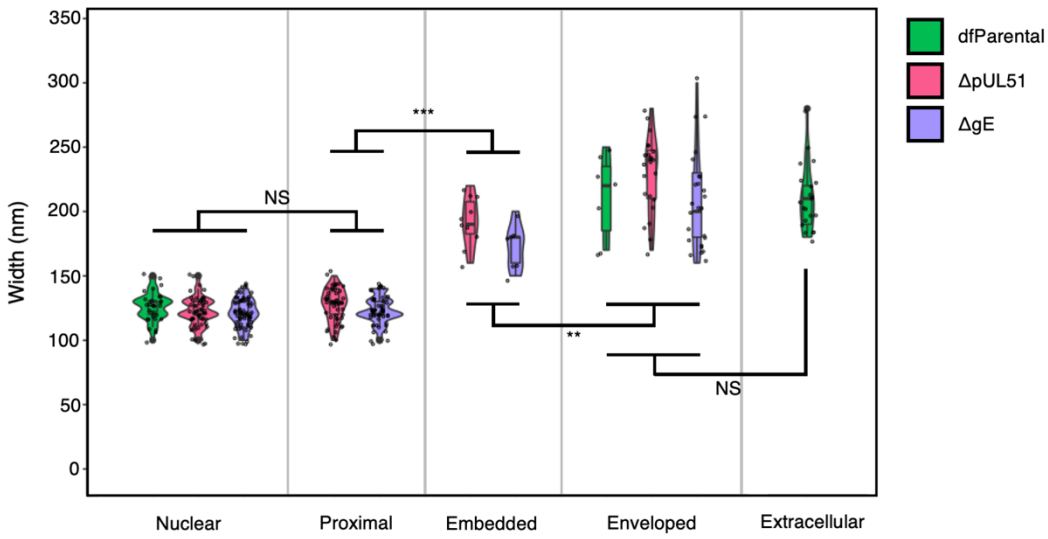

Figure 9. CryoSXT resolved differences in the widths of virus assembly intermediates. U2OS cells were infected at MOI = 2 for 16 hours. Widths of virus particles at different stages of assembly were measured for the dfParental, ΔpUL51, and ΔgE viruses. See Table 1 for values. Mann-Whitney *U* tests were used to assess the significance of differences. No significant differences in width were observed between virus mutants at the same stage of assembly except for enveloped ΔgE (N=25) and ΔpUL51 (N=22) virus assembly intermediates (p-value = 0.0285). P-value thresholds: <0.05 (*), <0.005 (**), and <0.0005 (***). NS, no significance. Scale bars = 1 µm.

1 **Table 1. Width of virus assembly intermediates measured using cryoSXT**

2 U2OS cells were infected at MOI = 2 for 16 hours. Data are combined from dfParental, ΔpUL51, and
3 ΔgE viruses. See Fig. 9 for a graphical representation. SD, standard deviation; SEM, standard error of
4 the mean; N, number of virus assembly intermediates used for analysis.

	mean	**SD**	**SEM**	**N**
Nuclear	122.5	11.4	0.9	149
Proximal	125.0	11.8	1.1	105
Embedded	184.1	20.0	4.9	17
Enveloped	216.9	34.2	4.7	54
Extracellular	210.0	25.9	5.6	21

5

References

1. Nicoll, M. P., Proença, J. T. & Efstathiou, S. The molecular basis of herpes simplex virus latency. *FEMS Microbiol. Rev.* **36**, 684–705 (2012).
2. Gatherer, D. *et al.* ICTV Virus Taxonomy Profile: Herpesviridae 2021. *J. Gen. Virol.* **102**, (2021).
3. Hernández Durán, A. *et al.* Protein interactions and consensus clustering analysis uncover insights into herpesvirus virion structure and function relationships. *PLOS Biol.* **17**, e3000316 (2019).
4. Owen, D., Crump, C. & Graham, S. Tegument Assembly and Secondary Envelopment of Alphaherpesviruses. *Viruses* **7**, 5084–5114 (2015).
5. Ahmad, I. & Wilson, D. W. HSV-1 Cytoplasmic Envelopment and Egress. *Int. J. Mol. Sci.* **21**, 5969 (2020).
6. Mettenleiter, T. C. Herpesvirus Assembly and Egress. *J. Virol.* **76**, 1537–1547 (2002).
7. Johnson, D. C. & Baines, J. D. Herpesviruses remodel host membranes for virus egress. *Nat. Rev. Microbiol.* **9**, 382–394 (2011).
8. Crump, C. Virus Assembly and Egress of HSV. in *Human Herpesviruses* (eds. Kawaguchi, Y., Mori, Y. & Kimura, H.) 23–44 (Springer Singapore, Singapore, 2018). doi:10.1007/978-981-10-7230-7_2.
9. Triezenberg, S. J., Kingsbury, R. C. & McKnight, S. L. Functional dissection of VP16, the trans-activator of herpes simplex virus immediate early gene expression. *Genes Dev.* **2**, 718–729 (1988).
10. Brown, J. C. & Newcomb, W. W. Herpesvirus capsid assembly: insights from structural analysis. *Curr. Opin. Virol.* **1**, 142–149 (2011).

11. Bigalke, J. M. & Heldwein, E. E. Structural basis of membrane budding by the nuclear egress complex of herpesviruses. *EMBO J.* **34**, 2921–2936 (2015).
12. Bigalke, J. M. & Heldwein, E. E. The Great (Nuclear) Escape: New Insights into the Role of the Nuclear Egress Complex of Herpesviruses. *J. Virol.* **89**, 9150–9153 (2015).
13. Bigalke, J. M. & Heldwein, E. E. Nuclear Exodus: Herpesviruses Lead the Way. *Annu. Rev. Virol.* **3**, 387–409 (2016).
14. Zeev-Ben-Mordehai, T. *et al.* Crystal Structure of the Herpesvirus Nuclear Egress Complex Provides Insights into Inner Nuclear Membrane Remodeling. *Cell Rep.* **13**, 2645–2652 (2015).
15. Hollinshead, M. *et al.* Endocytic tubules regulated by Rab GTPases 5 and 11 are used for envelopment of herpes simplex virus. *EMBO J.* **31**, 4204–4220 (2012).
16. Baines, J. D. & Roizman, B. The UL11 gene of herpes simplex virus 1 encodes a function that facilitates nucleocapsid envelopment and egress from cells. *J. Virol.* **66**, 5168–5174 (1992).
17. Fulmer, P. A., Melancon, J. M., Baines, J. D. & Kousoulas, K. G. UL20 Protein Functions Precede and Are Required for the UL11 Functions of Herpes Simplex Virus Type 1 Cytoplasmic Virion Envelopment. *J. Virol.* **81**, 3097–3108 (2007).
18. Le Sage, V. *et al.* The Herpes Simplex Virus 2 UL21 Protein Is Essential for Virus Propagation. *J. Virol.* **87**, 5904–5915 (2013).
19. Sarfo, A. *et al.* The UL21 Tegument Protein of Herpes Simplex Virus 1 Is Differentially Required for the Syncytial Phenotype. *J. Virol.* **91**, e01161-17 (2017).
20. Gao, J., Finnen, R. L., Sherry, M. R., Le Sage, V. & Banfield, B. W. Differentiating the Roles of UL16, UL21, and Us3 in the Nuclear Egress of Herpes Simplex Virus Capsids. *J. Virol.* **94**, (2020).

21. Mossman, K. L., Sherburne, R., Lavery, C., Duncan, J. & Smiley, J. R. Evidence that Herpes Simplex Virus VP16 Is Required for Viral Egress Downstream of the Initial Envelopment Event. *J. Virol.* **74**, 6287–6299 (2000).
22. Gunning, W. T. & Calomeni, E. P. A Brief Review of Transmission Electron Microscopy and Applications in Pathology. *J. Histotechnol.* **23**, 237–246 (2000).
23. Bråten, T. High Resolution Scanning Electron Microscopy in Biology: Artefacts Caused By the Nature and Mode of Application of the Coating Material. *J. Microsc.* **113**, 53–59 (1978).
24. Schauflinger, M., Villinger, C. & Walther, P. Three-Dimensional Visualization of Virus-Infected Cells by Serial Sectioning: An Electron Microscopic Study Using Resin Embedded Cells. in *Virus-Host Interactions* (eds. Bailer, S. M. & Lieber, D.) vol. 1064 227–237 (Humana Press, Totowa, NJ, 2013).
25. Kounatidis, I. *et al.* 3D Correlative Cryo-Structured Illumination Fluorescence and Soft X-ray Microscopy Elucidates Reovirus Intracellular Release Pathway. *Cell* **182**, 515-530.e17 (2020).
26. Nahas, K. L. *et al.* Near-native state imaging by cryo-soft-X-ray tomography reveals remodelling of multiple cellular organelles during HSV-1 infection. *PLOS Pathog.* (2022) doi:10.1101/2021.10.11.463900.
27. Douglas, M. W. *et al.* Herpes Simplex Virus Type 1 Capsid Protein VP26 Interacts with Dynein Light Chains RP3 and Tctex1 and Plays a Role in Retrograde Cellular Transport. *J. Biol. Chem.* **279**, 28522–28530 (2004).
28. Albecka, A., Laine, R. F., Janssen, A. F. J., Kaminski, C. F. & Crump, C. M. HSV-1 Glycoproteins Are Delivered to Virus Assembly Sites Through Dynamin-Dependent Endocytosis. *Traffic* **17**, 21–39 (2016).

29. Scherer, K. M. *et al.* A fluorescent reporter system enables spatiotemporal analysis of host cell modification during herpes simplex virus-1 replication. *J. Biol. Chem.* **296**, 100236 (2021).
30. Heilingloh, C. S. & Krawczyk, A. Role of L-Particles during Herpes Simplex Virus Infection. *Front. Microbiol.* **8**, 2565 (2017).
31. Chi, J. H. I. & Wilson, D. W. ATP-Dependent Localization of the Herpes Simplex Virus Capsid Protein VP26 to Sites of Procapsid Maturation. *J. Virol.* **74**, 1468–1476 (2000).
32. Foster, T. P., Melancon, J. M., Olivier, T. L. & Kousoulas, K. G. Herpes Simplex Virus Type 1 Glycoprotein K and the UL20 Protein Are Interdependent for Intracellular Trafficking and *trans* -Golgi Network Localization. *J. Virol.* **78**, 13262–13277 (2004).
33. Benedyk, T. H. *et al.* pUL21 is a viral phosphatase adaptor that promotes herpes simplex virus replication and spread. *PLOS Pathog.* **17**, e1009824 (2021).
34. Polcicova, K., Goldsmith, K., Rainish, B. L., Wisner, T. W. & Johnson, D. C. The Extracellular Domain of Herpes Simplex Virus gE Is Indispensable for Efficient Cell-to-Cell Spread: Evidence for gE/gI Receptors. *J. Virol.* **79**, 11990–12001 (2005).
35. Wisner, T. W. & Johnson, D. C. Redistribution of Cellular and Herpes Simplex Virus Proteins from the Trans-Golgi Network to Cell Junctions without Enveloped Capsids. *J. Virol.* **78**, 11519–11535 (2004).
36. Farnsworth, A., Goldsmith, K. & Johnson, D. C. Herpes Simplex Virus Glycoproteins gD and gE/gI Serve Essential but Redundant Functions during Acquisition of the Virion Envelope in the Cytoplasm. *J. Virol.* **77**, 8481–8494 (2003).
37. Han, J., Chadha, P., Starkey, J. L. & Wills, J. W. Function of glycoprotein E of herpes simplex virus requires coordinated assembly of three tegument proteins on its cytoplasmic tail. *Proc. Natl. Acad. Sci.* **109**, 19798–19803 (2012).

38. Klupp, B. G., Böttcher, S., Granzow, H., Kopp, M. & Mettenleiter, T. C. Complex Formation between the UL16 and UL21 Tegument Proteins of Pseudorabies Virus. *J. Virol.* **79**, 1510–1522 (2005).
39. Meckes, D. G., Marsh, J. A. & Wills, J. W. Complex mechanisms for the packaging of the UL16 tegument protein into herpes simplex virus. *Virology* **398**, 208–213 (2010).
40. Yeh, P.-C. *et al.* Direct and Specific Binding of the UL16 Tegument Protein of Herpes Simplex Virus to the Cytoplasmic Tail of Glycoprotein E. *J. Virol.* **85**, 9425–9436 (2011).
41. Benedyk, T. H. *et al.* Herpes simplex virus 1 protein pUL21 alters ceramide metabolism by activating the interorganelle transport protein CERT. *J. Biol. Chem.* **298**, 102589 (2022).
42. Farnsworth, A., Wisner, T. W. & Johnson, D. C. Cytoplasmic Residues of Herpes Simplex Virus Glycoprotein gE Required for Secondary Envelopment and Binding of Tegument Proteins VP22 and UL11 to gE and gD. *J. Virol.* **81**, 319–331 (2007).
43. Pražák, V. *et al.* Molecular plasticity of herpesvirus nuclear egress analysed in situ. *Nat. Microbiol.* **9**, 1842–1855 (2024).
44. Draganova, E. B., Thorsen, M. K. & Heldwein, E. E. Nuclear Egress. *Curr. Issues Mol. Biol.* **41**, 125–170 (2021).
45. Muradov, J. H., Finnen, R. L., Gulak, M. A., Hay, T. J. M. & Banfield, B. W. pUL21 regulation of pUs3 kinase activity influences the nature of nuclear envelope deformation by the HSV-2 nuclear egress complex. *PLOS Pathog.* **17**, e1009679 (2021).
46. Thorsen, M. K. *et al.* Highly Basic Clusters in the Herpes Simplex Virus 1 Nuclear Egress Complex Drive Membrane Budding by Inducing Lipid Ordering. *mBio* **12**, e01548-21 (2021).

47. Lau, S.-Y. & Crump, C. HSV-1 gM and the gK/pUL20 Complex Are Important for the Localization of gD and gH/L to Viral Assembly Sites. *Viruses* **7**, 915–938 (2015).
48. Butt, B. G. *et al.* Insights into herpesvirus assembly from the structure of the pUL7:pUL51 complex. *eLife* **9**, e53789 (2020).
49. Albecka, A. *et al.* Dual Function of the pUL7-pUL51 Tegument Protein Complex in Herpes Simplex Virus 1 Infection. *J. Virol.* **91**, (2017).
50. Svobodova, S., Bell, S. & Crump, C. M. Analysis of the Interaction between the Essential Herpes Simplex Virus 1 Tegument Proteins VP16 and VP1/2. *J. Virol.* **86**, 473–483 (2012).
51. Chen, J.-H. *et al.* Soft X-ray Tomography Reveals HSV-1-Induced Remodeling of Human B Cells. *Viruses* **14**, 2651 (2022).
52. Simpson-Holley, M., Colgrove, R. C., Nalepa, G., Harper, J. W. & Knipe, D. M. Identification and Functional Evaluation of Cellular and Viral Factors Involved in the Alteration of Nuclear Architecture during Herpes Simplex Virus 1 Infection. *J. Virol.* **79**, 12840–12851 (2005).
53. Deng, Z. *et al.* HSV-1 Remodels Host Telomeres to Facilitate Viral Replication. *Cell Rep.* **9**, 2263–2278 (2014).
54. Okolo, C. A. *et al.* Sample preparation strategies for efficient correlation of 3D SIM and soft X-ray tomography data at cryogenic temperatures. *Nat. Protoc.* **16**, 2851–2885 (2021).
55. Drayman, N., Patel, P., Vistain, L. & Tay, S. HSV-1 single-cell analysis reveals the activation of anti-viral and developmental programs in distinct sub-populations. *eLife* **8**, e46339 (2019).
56. Vyas, N. *et al.* Cryo-Structured Illumination Microscopic Data Collection from Cryogenically Preserved Cells. *J. Vis. Exp.* 62274 (2021) doi:10.3791/62274.

57. Gao, J., Hay, T. J. M. & Banfield, B. W. The Product of the Herpes Simplex Virus 2 UL16 Gene Is Critical for the Egress of Capsids from the Nuclei of Infected Cells. *J. Virol.* **91**, (2017).
58. Naldinho-Souto, R., Browne, H. & Minson, T. Herpes Simplex Virus Tegument Protein VP16 Is a Component of Primary Enveloped Virions. *J. Virol.* **80**, 2582–2584 (2006).
59. Leege, T. *et al.* Effects of Simultaneous Deletion of pUL11 and Glycoprotein M on Virion Maturation of Herpes Simplex Virus Type 1. *J. Virol.* **83**, 896–907 (2009).
60. Oda, S., Arii, J., Koyanagi, N., Kato, A. & Kawaguchi, Y. The Interaction between Herpes Simplex Virus 1 Tegument Proteins UL51 and UL14 and Its Role in Virion Morphogenesis. *J. Virol.* **90**, 8754–8767 (2016).
61. Hutchinson, L. & Johnson, D. C. Herpes simplex virus glycoprotein K promotes egress of virus particles. *J. Virol.* **69**, 5401–5413 (1995).
62. Finnen, R. & Banfield, B. CRISPR/Cas9 Mutagenesis of UL21 in Multiple Strains of Herpes Simplex Virus Reveals Differential Requirements for pUL21 in Viral Replication. *Viruses* **10**, 258 (2018).
63. Shahin, F. *et al.* Bovine herpesvirus 1 tegument protein *UL21* plays critical roles in viral secondary envelopment and cell-to-cell spreading. *Oncotarget* **8**, 94462–94480 (2017).
64. Lee, G. E., Murray, J. W., Wolkoff, A. W. & Wilson, D. W. Reconstitution of Herpes Simplex Virus Microtubule-Dependent Trafficking In Vitro. *J. Virol.* **80**, 4264–4275 (2006).
65. Maurer, U. E., Sodeik, B. & Grünewald, K. Native 3D intermediates of membrane fusion in herpes simplex virus 1 entry. *Proc. Natl. Acad. Sci.* **105**, 10559–10564 (2008).
66. Harkiolaki, M. *et al.* Cryo-soft X-ray tomography: using soft X-rays to explore the ultrastructure of whole cells. *Emerg. Top. Life Sci.* **2**, 81–92 (2018).

67. Wolf, D., Lubk, A. & Lichte, H. Weighted simultaneous iterative reconstruction technique for single-axis tomography. *Ultramicroscopy* **136**, 15–25 (2014).

68. Nahas, K. L., Ferreira Fernandes, J., Crump, C., Graham, S. C. & Harkiolaki, M. Contour: a semi-automated segmentation and quantitation tool for cryo-soft-X-ray tomography. *Biol. Imaging* **2**, (2022).

69. Maringer, K., Stylianou, J. & Elliott, G. A Network of Protein Interactions around the Herpes Simplex Virus Tegument Protein VP22. *J. Virol.* **86**, 12971–12982 (2012).

70. Grünewald, K. *et al.* Three-Dimensional Structure of Herpes Simplex Virus from Cryo-Electron Tomography. *Science* **302**, 1396–1398 (2003).

71. Henaff, D., Rémillard-Labrosse, G., Loret, S. & Lippé, R. Analysis of the Early Steps of Herpes Simplex Virus 1 Capsid Tegumentation. *J. Virol.* **87**, 4895–4906 (2013).

72. Bucks, M. A., O'Regan, K. J., Murphy, M. A., Wills, J. W. & Courtney, R. J. Herpes simplex virus type 1 tegument proteins VP1/2 and UL37 are associated with intranuclear capsids. *Virology* **361**, 316–324 (2007).

73. Mou, F., Wills, E. & Baines, J. D. Phosphorylation of the U(L)31 protein of herpes simplex virus 1 by the U(S)3-encoded kinase regulates localization of the nuclear envelopment complex and egress of nucleocapsids. *J. Virol.* **83**, 5181–5191 (2009).

74. Masoud Bahnamiri, M. & Roller, R. J. Mechanism of Nuclear Lamina Disruption and the Role of pUS3 in Herpes Simplex Virus 1 Nuclear Egress. *J. Virol.* **95**, e02432-20 (2021).

75. Bjerke, S. L. & Roller, R. J. Roles for herpes simplex virus type 1 UL34 and US3 proteins in disrupting the nuclear lamina during herpes simplex virus type 1 egress. *Virology* **347**, 261–276 (2006).

76. Gao, J., Yan, X. & Banfield, B. W. Comparative Analysis of *UL16* Mutants Derived from Multiple Strains of Herpes Simplex Virus 2 (HSV-2) and HSV-1 Reveals Species-Specific Requirements for the UL16 Protein. *J. Virol.* **92**, e00629-18 (2018).
77. Thomas, E. C. M., Bossert, M. & Banfield, B. W. The herpes simplex virus tegument protein pUL21 is required for viral genome retention within capsids. *PLoS Pathog.* **18**, e1010969 (2022).
78. Campbell, M. E. M., Palfreyman, J. W. & Preston, C. M. Identification of herpes simplex virus DNA sequences which encode a trans-acting polypeptide responsible for stimulation of immediate early transcription. *J. Mol. Biol.* **180**, 1–19 (1984).
79. Knez, J., Bilan, P. T. & Capone, J. P. A Single Amino Acid Substitution in Herpes Simplex Virus Type 1 VP16 Inhibits Binding to the Virion Host Shutoff Protein and Is Incompatible with Virus Growth. *J. Virol.* **77**, 2892–2902 (2003).
80. Ko, D. H., Cunningham, A. L. & Diefenbach, R. J. The Major Determinant for Addition of Tegument Protein pUL48 (VP16) to Capsids in Herpes Simplex Virus Type 1 Is the Presence of the Major Tegument Protein pUL36 (VP1/2). *J. Virol.* **84**, 1397–1405 (2010).
81. Elliott, G., Mouzakitis, G. & O'Hare, P. VP16 interacts via its activation domain with VP22, a tegument protein of herpes simplex virus, and is relocated to a novel macromolecular assembly in coexpressing cells. *J. Virol.* **69**, 7932–7941 (1995).
82. Gross, S. T., Harley, C. A. & Wilson, D. W. The cytoplasmic tail of Herpes simplex virus glycoprotein H binds to the tegument protein VP16 in vitro and in vivo. *Virology* **317**, 1–12 (2003).
83. Kamen, D. E., Gross, S. T., Girvin, M. E. & Wilson, D. W. Structural Basis for the Physiological Temperature Dependence of the Association of VP16 with the Cytoplasmic Tail of Herpes Simplex Virus Glycoprotein H. *J. Virol.* **79**, 6134–6141 (2005).

84. Kato, K. *et al.* Synthesis, subcellular localization and VP16 interaction of the herpes simplex virus type 2 UL46 gene product. *Arch. Virol.* **145**, 2149–2162 (2000).

85. Smibert, C. A., Popova, B., Xiao, P., Capone, J. P. & Smiley, J. R. Herpes simplex virus VP16 forms a complex with the virion host shutoff protein vhs. *J. Virol.* **68**, 2339–2346 (1994).

86. Schmelter, J., Knez, J., Smiley, J. R. & Capone, J. P. Identification and characterization of a small modular domain in the herpes simplex virus host shutoff protein sufficient for interaction with VP16. *J. Virol.* **70**, 2124–2131 (1996).

87. Farnsworth, A. & Johnson, D. C. Herpes Simplex Virus gE/gI Must Accumulate in the *trans* -Golgi Network at Early Times and Then Redistribute to Cell Junctions To Promote Cell-Cell Spread. *J. Virol.* **80**, 3167–3179 (2006).

88. Johnson, D. C., Webb, M., Wisner, T. W. & Brunetti, C. Herpes Simplex Virus gE/gI Sorts Nascent Virions to Epithelial Cell Junctions, Promoting Virus Spread. *J. Virol.* **75**, 821–833 (2001).

89. Roller, R. J. & Fetters, R. The Herpes Simplex Virus 1 UL51 Protein Interacts with the UL7 Protein and Plays a Role in Its Recruitment into the Virion. *J. Virol.* **89**, 3112–3122 (2015).

90. Crump, C. M., Yates, C. & Minson, T. Herpes Simplex Virus Type 1 Cytoplasmic Envelopment Requires Functional Vps4. *J. Virol.* **81**, 7380–7387 (2007).

91. Chouljenko, D. V. *et al.* Herpes Simplex Virus 1 UL37 Protein Tyrosine Residues Conserved among All Alphaherpesviruses Are Required for Interactions with Glycoprotein K, Cytoplasmic Virion Envelopment, and Infectious Virus Production. *J. Virol.* **90**, 10351–10361 (2016).

92. Jambunathan, N. *et al.* Herpes Simplex Virus 1 Protein UL37 Interacts with Viral Glycoprotein gK and Membrane Protein UL20 and Functions in Cytoplasmic Virion Envelopment. *J. Virol.* **88**, 5927–5935 (2014).

93. Gierasch, W. W. *et al.* Construction and characterization of bacterial artificial chromosomes containing HSV-1 strains 17 and KOS. *J. Virol. Methods* **135**, 197–206 (2006).

94. Tischer, B. K., Smith, G. A. & Osterrieder, N. En Passant Mutagenesis: A Two Step Markerless Red Recombination System. in *In Vitro Mutagenesis Protocols* (ed. Braman, J.) vol. 634 421–430 (Humana Press, Totowa, NJ, 2010).

95. Roller, R. J., Yuping, Z., Schnetzer, R., Ferguson, J. & DeSalvo, D. Herpes Simplex Virus Type 1 UL34 Gene Product Is Required for Viral Envelopment. *J. Virol.* **74**, 117–129 (2000).

96. Weinheimer, S. P., Boyd, B. A., Durham, S. K., Resnick, J. L. & O'Boyle, D. R. Deletion of the VP16 open reading frame of herpes simplex virus type 1. *J. Virol.* **66**, 258–269 (1992).

97. Carmichael, J. C. & Wills, J. W. Differential Requirements for gE, gI, and UL16 among Herpes Simplex Virus 1 Syncytial Variants Suggest Unique Modes of Dysregulating the Mechanism of Cell-to-Cell Spread. *J. Virol.* **93**, e00494-19 (2019).

98. Reynolds, A. E., Wills, E. G., Roller, R. J., Ryckman, B. J. & Baines, J. D. Ultrastructural Localization of the Herpes Simplex Virus Type 1 U_L 31, U_L 34, and U_S 3 Proteins Suggests Specific Roles in Primary Envelopment and Egress of Nucleocapsids. *J. Virol.* **76**, 8939–8952 (2002).

99. McLean, C. *et al.* Monoclonal Antibodies to Three Non-glycosylated Antigens of Herpes Simplex Virus Type 2. *J. Gen. Virol.* **63**, 297–305 (1982).

100. Finnen, R. L., Roy, B. B., Zhang, H. & Banfield, B. W. Analysis of filamentous process induction and nuclear localization properties of the HSV-2 serine/threonine kinase Us3. *Virology* **397**, 23–33 (2010).

101. Cross, A. M., Hope, R. G. & Marsden, H. S. Generation and Properties of the Glycoprotein E-related 32K/34K/35K and 55K/57K Polypeptides Encoded by Herpes Simplex Virus Type 1. *J. Gen. Virol.* **68**, 2093–2104 (1987).

102. McClelland, D. A. *et al.* pH Reduction as a Trigger for Dissociation of Herpes Simplex Virus Type 1 Scaffolds. *J. Virol.* **76**, 7407–7417 (2002).

103. Pierce, K. E., Rice, J. E., Sanchez, J. A. & Wangh, L. J. QuantiLyse ™ : Reliable DNA Amplification from Single Cells. *BioTechniques* **32**, 1106–1111 (2002).

104. Macdonald, S. J., Mostafa, H. H., Morrison, L. A. & Davido, D. J. Genome Sequence of Herpes Simplex Virus 1 Strain KOS. *J. Virol.* **86**, 6371–6372 (2012).

105. Sievers, F. & Higgins, D. G. Clustal Omega. *Curr. Protoc. Bioinforma.* **48**, (2014).

106. Waterhouse, A. M., Procter, J. B., Martin, D. M. A., Clamp, M. & Barton, G. J. Jalview Version 2--a multiple sequence alignment editor and analysis workbench. *Bioinformatics* **25**, 1189–1191 (2009).

107. Minson, A. C. *et al.* An Analysis of the Biological Properties of Monoclonal Antibodies against Glycoprotein D of Herpes Simplex Virus and Identification of Amino Acid Substitutions that Confer Resistance to Neutralization. *J. Gen. Virol.* **67**, 1001–1013 (1986).

108. Rueden, C. T. *et al.* ImageJ2: ImageJ for the next generation of scientific image data. *BMC Bioinformatics* **18**, 529 (2017).

109. Schindelin, J. *et al.* Fiji: an open-source platform for biological-image analysis. *Nat. Methods* **9**, 676–682 (2012).

110. Phillips, M. A. *et al.* CryoSIM: super-resolution 3D structured illumination cryogenic fluorescence microscopy for correlated ultrastructural imaging. *Optica* **7**, 802 (2020).

111. Matsuda, A., Koujin, T., Schermelleh, L., Haraguchi, T. & Hiraoka, Y. High-Accuracy Correction of 3D Chromatic Shifts in the Age of Super-Resolution Biological Imaging Using Chromagnon. *J. Vis. Exp.* 60800 (2020) doi:10.3791/60800.

112. Mastronarde, D. N. & Held, S. R. Automated tilt series alignment and tomographic reconstruction in IMOD. *J. Struct. Biol.* **197**, 102–113 (2017).

113. Paul-Gilloteaux, P. *et al.* eC-CLEM: flexible multidimensional registration software for correlative microscopies. *Nat. Methods* **14**, 102–103 (2017).

114. Vyas, N. *et al.* Protocol for image registration of correlative soft X-ray tomography and super-resolution structured illumination microscopy images. *STAR Protoc.* **2**, 100529 (2021).

115. Gómez-Rubio, V. ggplot2 - Elegant Graphics for Data Analysis (2nd Edition). *J. Stat. Softw.* **77**, (2017).

116. Racine, J. S. RStudio: A Platform-Independent IDE for R and Sweave: Software Review. *J. Appl. Econom.* **27**, 167–172 (2012).

117. Lord, S. J., Velle, K. B., Mullins, R. D. & Fritz-Laylin, L. K. SuperPlots: Communicating reproducibility and variability in cell biology. *J. Cell Biol.* **219**, e202001064 (2020).

118. Negatsch, A., Mettenleiter, T. C. & Fuchs, W. Herpes simplex virus type 1 strain KOS carries a defective US9 and a mutated US8A gene. *J. Gen. Virol.* **92**, 167–172 (2011).

119. Foster, T. P., Alvarez, X. & Kousoulas, K. G. Plasma Membrane Topology of Syncytial Domains of Herpes Simplex Virus Type 1 Glycoprotein K (gK): the UL20 Protein Enables Cell Surface Localization of gK but Not gK-Mediated Cell-to-Cell Fusion. *J. Virol.* **77**, 499–510 (2003).

120. Ward, P. L., Ogle, W. O. & Roizman, B. Assemblons: nuclear structures defined by aggregation of immature capsids and some tegument proteins of herpes simplex virus 1. *J. Virol.* **70**, 4623–4631 (1996).

121. Lee, J. I.-H., Luxton, G. W. G. & Smith, G. A. Identification of an Essential Domain in the Herpesvirus VP1/2 Tegument Protein: the Carboxy Terminus Directs Incorporation into Capsid Assemblons. *J. Virol.* **80**, 12086–12094 (2006).